Preserved lipid signatures in palaeosols help to distinguish the impacts of palaeoclimate and indigenous peoples on palaeovegetation in northwest Siberia

Loïc Harrault, Karen Milek, Arnaud Huguet, Christelle Anquetil, David Anderson

Preserved lipid signatures in palaeosols help to distinguish the impacts of palaeoclimate and indigenous peoples on palaeovegetation in northwest Siberia

Loïc Harrault[a,b*], Karen Milek[a], Arnaud Huguet[b], Christelle Anquetil[b], David G. Anderson[c¶].

[a] *Department of Archaeology, Durham University, Durham, DH1 3LE, UK*

[b] *Sorbonne Université, CNRS, EPHE, PSL, UMR METIS, F-75005 Paris, France*

[c] *Department of Anthropology, University of Aberdeen, AB24 4QY, Aberdeen, Scotland*

*Correspondence to: loic.harrault@gmail.com

ABSTRACT

Arctic reindeer herders demonstrate resilience to climate fluctuations by adjusting their pastoral practices to changing environments. The multiple phases of occupation at one of the oldest identified reindeer-herding sites, Ï‍Arte 6 on the Ï‍Amal peninsula, northwest Siberia, are thought to be linked to its local vegetation cover. Here we provide information on local palaeovegetation and climate shifts which occurred between the 7th and the 11th century CE based on lipid biomarkers. Aliphatic compounds, pentacyclic triterpenoids, branched glycerol dialkyl glycerol tetraethers (brGDGTs) and other lipids were analysed in four separate palaeosols from two loess-palaeosol sequences at the site. Based on different indices, the impact of human- or root-derived lipids and post-depositional microbial degradation on the signature of the studied pedosequences seem limited, which indicates that palaeobiomarkers are well preserved and representative of the analysed compounds.

n-Alkanes, *n*-carboxylic acids, *n*-aldehydes and pentacyclic triterpenoids point to the progressive colonization of grasses, sedges and herbs at the site, which can be attributed to the regional decrease in temperature suggested by bacterial-derived brGDGTs. During the last phase of occupation, however, when proxies point to increasing temperatures, and shrubs would normally be expected to return, the shrub cover continued to decrease, probably due to the impact of camping and holding reindeer at the site. The decoupling trends observed for particular pentacyclic triterpenoids as potential dwarf birch biomarkers could suggest a preferential shift of species within shrubs, probably influenced by human activities. Multi-family lipid biomarker analysis therefore made it possible to distinguish anthropogenic impacts on the local vegetation cover from regional climatic changes, and show how significant the impacts of humans on local vegetation can be, even in extreme environments where such activities are limited.

Keywords: Geoarchaeology; Human-environment interactions; Palaeoenvironmental reconstruction; Tundra vegetation; Lipid biomarkers

1. Introduction

In tundra ecosystems, permafrost thawing caused by global warming is having dramatic impacts on flora and carbon release (Zimov et al., 2006). In addition, warmer temperatures and increased humidity due to more rapid evaporation of Arctic seas can induce dramatic climatic events such as the recent rain-on-snow events encountered in the Í̂Amal Peninsula of northwestern Siberia (Forbes et al., 2016). Rain-on-snow, which rapidly freezes to form an impenetrable ice cover, has considerable consequences for wildlife and domesticated reindeer, and consequently for the local indigenous Nenetses. Their reindeer-herding lifestyle is dependent on accessible winter food sources (lichen) for deer (Forbes et al., 2016). As such, understanding how Nenetses and their predecessors responded to climate variations over time is of primary importance for predicting the future of Arctic indigenous peoples. At the same time, herding reindeer (*Rangifer tarandus*) can have significant impacts on the local landscape, for example due to wood-cutting for fuel, shrub grazing, soil trampling and inputs of urine and faeces by reindeer (Olofsson, 2006; Skarin et al., 2020). As a result, it can be very complex to determine the causes of palaeoenvironmental changes on sites with a long human-animal-environment relationship history.

Recently, Anderson et al. (2019) studied the occupation history at Í̂Arte 6, an archaeological site on the Í̂Amal Peninsula, through the analysis of loess-palaeosol sequences in its immediate hinterland. This site, located in a region still used by local Nenetses, has been occupied several times since at least the 3th century CE. The combined anthropological, palynological, geoarchaeological and faecal lipid biomarker data led Anderson et al. (2019)

to suggest that the presence of human-reindeer groups began at the site at a modest scale, aimed mainly at hunting wild herds with just a few decoy deer. Over time, as the wild deer hunting and carcass-processing activities at the site intensified, ultimately resulting in the deposition of tens of thousands of reindeer bones and artefacts (Plekhanov, 2014; Nomokonova et al., 2018), reindeer-pulled sled transport became crucial for larger groups and their goods. The faecal lipid biomarker evidence around the site indicated an increase in the size of the domestic herds held there. This intensive phase of human and reindeer activity ca. 1000 years ago is thought to be responsible for the unusually lush grass that still covers the site today, which stands out sharply in a tundra landscape otherwise characterised by a sparse cover of tundra herbs, mosses, lichen and dwarf shrubs (Plekhanov, 2014).

One of the key unanswered questions about this site is why this particular location was repeatedly selected as a place to camp and eventually process large numbers of reindeer carcasses. Based on ethnographic analogies with modern reindeer hunters and herders, Anderson et al. (2019) suggested that the microtopography and vegetation cover at the site probably played major roles, including the availability of shrub wood for fires, shrub cover for hunting hides, and suitable pasture for reindeer. However, the palaeovegetation cover at this site is very difficult to reconstruct based on plant macro- and microfossils. The nearby peat bog, which was sampled and analysed for pollen in 2013, does not date as far back as the first millennium CE, while the lakes in the region, which do have sufficiently long sequences, provide only a broad regional picture with unclear palaeoclimatic trends (Anderson et al., 2019; Lake Three). Moreover, the next nearest lake-based Holocene palaeoenvironmental reconstructions were conducted further than 2000 km east of the Î‍Amal Peninsula, and at a kyr time scale resolution, preventing any comparison with the Î‍Arte archaeological context (Andreev et al., 2004, Müller et al., 2009). Previous to the current study, only pollen data

92 obtained from a monolith collected at Î Arte 6 from the excavation itself were available to
93 interpret the past vegetation cover, but this sequence was disturbed and covered a restricted
94 timeframe (Panova et al., 2008; Anderson et al., 2019). Therefore, the macro- and microplant
95 fossil records available to reconstruct the palaeovegetation at Î Arte 6 is incomplete and
96 requires additional corroborating evidence from the palaeosol sequences.
97 Compared to pollen, which can travel greater distances, biochemicals from plants,
98 especially lipids, can be associated with very localized inputs of soil organic matter (SOM)
99 by a progressive incorporation and physical degradation of local plant remains after decay
100 (Davies, 2000). Lipid-based palaeoenvironmental reconstructions using soils or sediments are
101 often based on *n*-alkanes, which can allow the identification of the main plant group sources
102 based on the distribution of long-chain homologues. However, the identification of
103 palaeovegetation using only *n*-alkane distributions in environmental archives can be complex
104 because of; (a) inter- and intra-plant species chemotaxonomic differences, (b) other sources
105 of *n*-alkanes in soil organic matter (SOM) such as plant roots, and (c) microbially driven
106 selective degradation of *n*-alkanes (Jansen and Wiesenberg, 2017; Thomas et al., 2021 and
107 references therein). Complementary information can be obtained from the study of other lipid
108 classes, and the potential effects of other sources of biomarkers (roots, human-derived
109 compounds, etc.) or post-depositional processes (e.g., microbial degradation) have to be taken
110 into account (Jansen and Wiesenberg, 2017).
111 In addition to palaeovegetation reconstruction, lipid biomarkers and related proxies can
112 also be used to infer past temperature change (Jansen and Wiesenberg, 2017). Among these
113 compounds, branched glycerol dialkyl glycerol tetraethers (brGDGTs) are a group of
114 membrane lipids produced by some bacteria, which are ubiquitously present in terrestrial and
115 aquatic environments. Their distribution in soils has been shown to be mainly dependent on

116 air temperature and soil pH (Weijers et al., 2007; De Jonge et al., 2014; Véquaud et al.,
117 2022), and they are now widely used to reconstruct past mean annual air temperatures (MAT)
118 in terrestrial environments (e.g., Rees-Owen et al., 2018).

119 In this study, various lipid biomarkers (*n*-alkyl compounds, pentacyclic triterpenoids and
120 brGDGTs) were analysed to reconstruct palaeovegetation and climate changes from two
121 loess-palaeosol sequences at the ÎArte 6 site (NW Siberia). The palaeoenvironmental changes
122 derived from lipid-based proxies were then compared to other local and regional
123 palynological and dendroclimatological records to disentangle human- from climate-induced
124 palaeovegetation shifts. Even though lipid biomarkers have previously been applied to soil-
125 sediment archives (Wiesenberg et al., 2015) and loess-palaeosol sequences (e.g., Zech et al.,
126 2012; Tarasov et al., 2013) to reconstruct Quaternary palaeoenvironments in Siberia, the
127 present study is the first one to investigate the potential human-animal impacts on the
128 environment at a Siberian archaeological site.

129

130 **2. Materials and methods**

131 *2.1. Site description and sampling strategy*

132 Detailed descriptions of the ÎArte 6 site, its surrounding landscape and associated
133 palaeosols can be found in Anderson et al. (2019) and Harrault et al. (2019). The site is
134 located on the western edge of a high and open terrace overlooking the southern floodplain of
135 the ÎUribei River in the ÎAmal Peninsula, northwest Siberia (Fig. 1). The modern mean
136 annual temperatures range between -5 and -10 °C, with snow and ice cover up to ten months
137 a year.

138

139 *2.1.1. Modern vegetation*

The site is located ca. 250 km north of the current tree line. The contemporary landscape at Î Arte 6 displays different types of vegetation over a span of a few dozen metres (Fig. 1), a level of variation consistent with that observed in the wider vicinity (Skarin et al., 2020; Verdonen et al., 2020). The modern vegetation cover was formally surveyed by Bruce Forbes during the summer of 1996, and has remained largely unchanged since then. It consists of an unusually lush grassy sward largely dominated by *Poceae* (quadrats 1 and 2 in Supplementary Table S1) on the western edge of the terrace, where the archaeological site is located, and on the slope below the site. Shrubs are almost entirely absent from this zone. East of the archaeological site is a disturbed sandy tundra meadow composed of lichens, mosses, grasses and very low shrubs (quadrat 4). Even further east is an ombrotrophic bog dominated by lichens (quadrat 5). Large patches of deciduous shrubs (*Betula nana, Salix* spp., etc.) are found on the lower part of the terrace slope (quadrat 6) as well as further west towards the mire (no quadrat number) and nearby oxbow lakes in the floodplain. North and south of the Î Arte 6 terrace is a typical tundra dwarf shrub habitat dominated by dwarf shrubs (*Betula nana, Ledum decumbens, Carex bigelowii*) and stunted shrubs (*Salix* spp).

2.1.2. Pedosequence description

The focus of the present study is the sandy tundra meadow east of the archaeological site, which contains discontinuous loess-palaeosol sequences (LPS) with buried A horizons (Ab, palaeosols) separated by aeolian (windblown) sandy silt. These were recorded and sampled using shovel test pits on a 10 m grid (subsequently reduced in one zone to 5 m for higher resolution), the full details of which are in Anderson et al. (2019). At several locations, the Ab horizons and/or their associated humic horizons (Ahb) contained charcoal, ceramic fragments, bone fragments and/or burnt bone fragments, which were associated with

164 temporary human occupation (Anderson et al., 2019). Due to frost-heave and incomplete or
165 irregular sealing of palaeosols, many test pits presented only two or three Ab horizons, while
166 the highest number of buried palaeosols found was four. These were located at two locations:
167 10/80 and 30/60, and the samples from the Ab horizons in these test pits were used for the
168 present study (Figs. 1 and 2).

169 The test pit located at 30/60 on the local grid contained a clear pedosequence with a
170 depth of 41 cm. It consisted of a succession of sandy silt or silty sand palaeosols and aeolian
171 deposits, all of which contained living roots (Fig. 2, Supplementary Table S2). Due to the
172 high surface magnetic susceptibility measurements, abundant pottery pieces, and wood
173 charcoal fragments, 30/60 was interpreted as the location of an annex campsite used before
174 and during the occupation of the main I͡Arte 6 site. As described in Anderson et al. (2019),
175 the calibrated radiocarbon dates on the largest charcoal pieces (*Betula* sp. and *Salix* sp.
176 roundwood) from each palaeosol (Fig. 2) spanned the 7th to 11th century CE.

177 In the 10/80 test pit, the four palaeosol horizons were distinguishable on the basis of
178 colour and boundaries, but there was no loess separating the upper two palaeosols (Ab1 and
179 Ab2) or the lower two (Ab3 and Ab4). This could be the result of wind erosion, but elevated
180 concentrations of phosphates and faecal lipid biomarkers (5β-stanols) at this location also
181 suggest that the soil could have been eroded by the localized congregation of reindeer, as was
182 observed at Nenets campsites throughout Siberia (Anderson et al., 2014; Harrault et al.,
183 2019). Living roots from grasses and dwarf shrubs were present in the four palaeosols
184 (Supplementary Table S2). No charcoal or artefacts were found in this pedosequence, making
185 it difficult to date independently.
186

187 *2.2. Sampling*

After photographing the freshly exposed soil profiles in each test pit and recording the depth, Munsell soil colour (Munsell Color Co., Inc., 1975), texture, structure and inclusions for each soil horizon (Supplementary Table S2), 50–500 g of fresh soil was collected from the buried A horizons, depending on their thickness (Fig. 2). The loess between the buried soils was not sampled from each test pit because the focus of the original sampling design was the identification of anthropogenic deposits/inclusions and faecal lipid biomarkers associated with the stable land surfaces (palaeosols). Soil samples were collected directly from the exposed soil profile on the edge of the test pit with a metal trowel or a spatula wiped with a clean paper tissue and rinsed with deionised water. The exposed surface of each palaeosol was sampled by scraping and bagging a few mm of soil from the whole thickness of the palaeohorizons identified as buried soils on the basis of their homogeneous colour, structure and texture (Fig. 2). Thus, each palaeosol sample was considered to be an integrated snapshot of palaeoenvironmental conditions while the whole of the horizon was forming. No field replicates were sampled. Soil samples were stored in ziplocked polyethylene bags for a few hours, before being taken to a field lab tent, where they were placed into hand-made foil basket for 48 h of air drying. Air-dried samples were sieved at 2 mm to remove bigger roots and pebbles and to retrieve charcoal and bone pieces, then sieved samples where repacked into plastic bags. After the month-long field season, samples were re-dried at the lab in an oven at 50 °C overnight before further treatment for lipid biomarker extraction.

2.3. Lipid analysis

Samples from each palaeosol (Ab1 to Ab4) from both test pits (30/60 and 10/80) were split into three sub-samples, which were each extracted and analysed independently, and then treated as triplicates (n = 3).

2.3.1. Sample preparation

Lipid extraction and separation procedures were adapted from Harrault et al. (2019). Approximately 4 g of dried, crushed and 250 µm-sieved soil samples were extracted three times by sonication with a dichloromethane (DCM)/methanol (MeOH) mixture (2:1, v/v), then centrifuged and filtered. Pooled and concentrated extracts were separated into apolar and polar fractions by solid-liquid chromatography in glass columns filled with silica: apolar fractions were eluted with *n*-heptane and a *n*-heptane/DCM mixture (2:1, v/v), then polar fractions were eluted with a DCM/MeOH mixture (2:1, v/v). Before analysis by GC–MS, deuterated *n*-alkane (d_{50}-C_{24}) and 5α-cholestane were added as internal standard (IS) to aliquots of concentrated apolar and polar fractions, respectively. The latter was derivatised with a mixture of N,O-bis-(trimethylsilyl)trifluoroacetamide and trimethylchlorosilane (BSTFA + TMCS, 99:1, v/v) at 70 °C for 30 min. For brGDGT analysis, a second aliquot of the polar fraction was centrifuged, dissolved in *n*-heptane and a known amount of a C_{46}-synthesized internal standard was added prior to analysis (Huguet et al., 2013).

2.3.2. Apolar fraction analysis

Apolar fractions were analysed by a gas chromatograph coupled with a mass spectrometer (GC–MS), Agilent GC6890N-MS5973N equipped with an Rxi-5Sil MS capillary column (Restek, 30 m × 0.25 mm i.d., 0.5 µm film thickness). 1 µl samples were injected in splitless mode at 280 °C. Helium was used as carrier gas and flow was set at 1 ml/min. The GC oven temperature program started at 50 °C, increased to 320 °C at 4 °C/min, and held for 15 min. The transfer line temperature was set at 310 °C and EI voltage at 70 eV. Analyses were carried in full scan mode (*m*/*z* 35–700). Biomarkers were identified from mass

spectra and GC retention times. Semi-quantification was achieved by comparison of compound total ion current (TIC) peak area with those of the internal standard and expressed as relative abundance (%) compared to the sum of all integrated compounds within the fraction. Within each compound family, compound variations were expressed as their relative abundance compared to the sum of compound within the family considered.

2.3.3. Polar fraction analyses

Polar compounds were analysed with the same GC–MS instrument and capillary column as the apolar fractions. 1 µl of derivatised fractions were injected at 280 °C in split mode (10 ml/min) with a constant 1 ml/min flow of helium as the carrier gas. The GC oven temperature program started at 60 °C, increased to 150 °C at 15 °C/min, then increased to 310 °C at 3 °C/min and was held for 20 min. The transfer line temperature was set at 310 °C and EI voltage at 70 eV. Analyses were conducted in full scan mode (*m*/*z* 35–700). Compounds were identified from mass spectra and GC retention times. Semi-quantification was achieved by comparison of their TIC peak area with those of the IS (5α-cholestane) and expressed as the relative abundance of compound families and compounds within each family, as for apolar fractions.

GDGT analyses were performed using high performance liquid chromatography-atmospheric pressure chemical ionisation-mass spectrometry (HPLC–APCI-MS) with a Shimadzu LCMS-2020, as described by Huguet et al. (2019). Briefly, separation was achieved with two Hypersil Gold silica columns (Thermo Scientific, 150 mm × 2.1 mm, 1.9 µm) mounted in series at 40 °C, using different proportions of hexane and hexane/isopropanol (9:1, v/v) at 0.2 ml/min. This method allows the separation of 5-methyl and 6-methyl brGDGT isomers. The injection volume was 30 µl. Detection was performed in

selected ion monitoring mode, targeting the protonated molecules at *m/z* 744, 1018, 1020, 1022, 1032, 1034, 1036, 1046, 1048 and 1050. Semi-quantification of the GDGTs was performed by comparing the integrated signal of the respective compound with the signal of the internal standard previously added, as described by Huguet et al. (2013).

2.4. Lipid proxies used for palaeoenvironmental reconstruction

n-Alkane odd-over-even predominance (OEP) was calculated as follows (Zech et al., 2009):

$$OEP = (C_{25} + C_{27} + C_{29} + C_{31} + C_{33}) / (C_{26} + C_{28} + C_{30} + C_{32}) \quad (1)$$

In equation 1 and following, C_i represents the relative contribution of the homologue with an i-long carbon chain compared to the sum of the homologous series.

n-Alkane carbon preference index (CPI) was calculated as follows (Wiesenberg et al., 2015):

$$CPI = ([(C_{25} + C_{27} + C_{29} + C_{31} + C_{33})/(C_{24} + C_{26} + C_{28} + C_{30} + C_{32})] + [([(C_{25} + C_{27} + C_{29} + C_{31} + C_{33}) / (C_{26} + C_{28} + C_{30} + C_{32} + C_{34})])/2 \quad (2)$$

n-Alkane composition/carbon chain diversity index (CDI) was calculated as in Hjulström and Isaksson (2009):

$$CDI = 1/\sqrt{(\Sigma[C_i/100]^2)} \quad (3)$$

n-Alkanoic acid even-over-odd predominance (EOP) was calculated as follows (Schäfer et al., 2016):

$$EOP = (C_{24} + C_{26} + C_{28} + C_{30} + C_{32})/(C_{23} + C_{25} + C_{27} + C_{29} + C_{31}) \quad (4)$$

Palaeovegetation indices based on *n*-alkanoic acid distributions were calculated according to Schäfer et al. (2016):

$$\text{Deciduous trees, Index D: } C_{28}/(C_{24} + C_{28} + C_{32} + C_{34}) \quad (5)$$

Grasses, Index G: $(C_{32} + C_{34})/(C_{24} + C_{28} + C_{32} + C_{34})$ (6)

The ratio of saturated over unsaturated C_{16} and C_{18} fatty acids was used as a proxy for microbial degradation of native SOM (Wiesenberg et al., 2015):

FA C_{16+18} sat./unsat.= $(C_{16:0} + C_{18:0})$ $(\Sigma C_{16:1} + \Sigma C_{18:1} + C_{18:2})$ (7)

With $\Sigma C_{16:1}$ and $\Sigma C_{18:1}$ representing respectively the sum of the different monounsaturated homologues of $C_{16:1}$ and $C_{18:1}$.

The *n*-aldehyde C_{26}/C_{28} ratio was calculated as a possible proxy for palaeovegetation based on the results in van Bergen et al. (1997) displaying the presence of the C_{28} homologues in some tree and shrub leave species and its absence in grasses and herbs.

In the environment, Δ^5-sterols are mainly converted into their saturated counterparts (5α-stanols) by in situ microbial hydrogenation, thus Δ^5-sterol/5α-stanol ratios can be used as proxies for microbial degradation of the native lipid signal (Gaskell and Eglinton, 1976). Here, we used the sitosterol/sitostanol (24-ethylcholest-5-en-3β-ol/24-ethyl-5α-cholestan-3β-ol) ratio as sitosterol is the main phytosterol found in most plants.

As the concomitant occurrence of betulin, betulinic acid, lupeol and lupenone are used as markers for *Betulaceae* plant species in soil archive or archaeological material (Regert and Rolando, 2002; Modugno et al., 2006), the sum of their respective abundances in SOM was used in the present study as a proxy for *Betulaceae* contributions to palaeovegetation.

Mean annual palaeotemperatures (MAT) were reconstructed from brGDGTs using different soil calibrations.

Weijers et al. (2007):

MAT_{MBT} (°C) = (MBT – 0.122 – [0.187 × CBT])/0.02 (8)

with:

CBT = – log [(Ib + IIb)/(Ia + IIa)] (9)

$$MBT = (Ia + Ib + Ic)/(Ia + Ib + Ic + IIa + IIb + IIc + IIIa + IIIb + IIIc) \quad (10)$$

Peterse et al. (2012):

$$MAT_{MBT'}\ (°C) = 0.81 - (5.67 \times CBT) + (31 \times MBT') \quad (11)$$

with:

$$MBT' = (Ia + Ib + Ic) / (Ia + Ib + Ic + IIa + IIb + IIc + IIIa) \quad (12)$$

De Jonge et al. (2014):

$$MAT_{5Me}\ (°C) = -8.57 + (31.45 \times MBT') \quad (13)$$

$$MAT_{mr}\ (°C) = 7.17 + (17.1 \times Ia) + (25.9 \times Ib) + (34.4 \times Ic) - (28.6 \times IIa) \quad (14)$$

Roman numbers in equations 8–14 refer to the relative abundances of brGDGTs as presented in De Jonge et al. (2014) compared to their sum (Supplementary Fig. S1). It should be noted that only 5-methyl brGDGTs were detected in the soil samples of the two sequences investigated in this study.

Local plant (aerial parts and roots) lipids were not analysed in the present study. We compared our SOM lipid data to those of Ronkainen et al. (2015), which analysed the lipid composition (mainly *n*-alkanes) of above- and below-ground plant parts from a site located in a similar biome with a similar plant species as ÎArte 6's, ca. 300 km to the southwest. Some *n*-alkane-derives proxies such as CDI or OEP, not originally presented in Ronkainen et al. (2015), were calculated here.

3. Results

3.1. Lipid composition

The different lipid compounds found in soil samples from both test pits, as well as their respective chromatographic and spectral information, can be found in Supplementary Table S3. In both test pits 10/80 and 30/60, the apolar fractions were dominated by *n*-alkanes (77 ±

21% and 48 ± 15% of total apolar compounds, respectively; Fig. 3) and also contained significant amounts of *n*-aldehydes (10 ± 8% and 40 ± 15%) and triterpenoid hydrocarbons (12 ± 14% and 12 ± 6%), and to a much lower extent polycyclic aromatic hydrocarbons (less than 1% for both sequences). Polar fractions from both pedosequences were quite similar and were dominated by *n*-alkanoic acids (fatty acids or FA; 40 ± 1% of total polar compounds for both sequences; Fig. 3), followed by *n*-alkanols (OH; 20 ± 1%) and α,ω-hydroxy alkanoic acids (OH-FA; 20 ± 1% for 10/80 and 18 ± 1% for 30/60), functionalised pentacyclic triterpenoids (6 ± 1% for 10/80 and 8 ± 1% for 30/60) , α,ω-alkanedioic acids (di-FA; 5 ± 1% for both profiles), steroids (5 ± 0% for 10/80 and 3 ± 0% for 30/60), glycerides (mono-, di-, tri-acylglycerols (2 ± 0%); , *n*-alkan-2-one (2 ± 0%), α,(ω-1)-alkanediols (1 ± 0%) and other miscellaneous and unknown/unidentified compounds (e.g., *n*-amides, phenol derivatives, sugars etc.) accounted for less than 1% of polar compounds.

Additional lipid distributions are available in Supplementary Figs. S2 and S5 and Supplementary Material S1.

3.2. n-Alkanes

In the four buried horizons (Ab1 to Ab4) from both pedosequences, the *n*-alkane distribution ranged from C_{17} to C_{35} with a strong OEP predominance, a skewed unimodal distribution maximizing at C_{31} and a clear predominance of long chain homologues (ACL > 27; Supplementary Fig. S2). In sequence 10/80, OEP values increase from 7.7 ± 0.3 at Ab1 to 14.9 ± 1.0 at Ab4 (Fig. 4a,b). In sequence 30/60, OEP values generally increase with depth and range from 8.7 ± 0.5 (Ab1) to 11.4 ± 0.9 (Ab3). In the 10/80 sequence, CDI values decrease with depth between each palaeosol from 2.7 ± 0.0 (Ab1) to 1.9 ± 0.0 (Ab4). The decrease with depth of the CDI proxy along the 30/60 sequence is less pronounced with

values ranging from 2.4 ± 0.1 (Ab1) to 2.2 ± 0.1 (Ab3 and Ab4). In the 10/80 sequence the C_{23}/C_{25} and C_{23}/C_{27} ratio values display similar trends with an initial decrease from Ab1 (0.68 ± 0.02 and 0.32 ± 0.01, respectively) to Ab2 (0.51 ± 0.01 and 0.23 ± 0.01), followed by a slight decrease from Ab2 to Ab3 (0.50 ± 0.02 and 0.21 ± 0.01), then eventually increases from Ab3 to Ab4 (0.57 ± 0.01 and 0.25 ± 0.00). In the 30/60 sequence, the values of the C_{23}/C_{25} and C_{23}/C_{27} ratio values decrease from Ab1 (0.54 ± 0.02 and 0.28 ± 0.01, respectively) to Ab3 (0.47 ± 0.02 and 0.22 ± 0.01), and the trend between Ab3 and Ab4 is unclear due to a large standard deviation found in Ab4 samples. Overall, C_{31}/C_{27} and C_{33}/C_{27} ratios decrease with depth in both partial pedosequences, with values ranging respectively from 1.61 ± 0.03 and 0.31 ± 0.01 (Ab1) to 8.26 ± 0.16 and 2.00 ± 0.14 (Ab4) along the 10/80 profiles and from 2.44 ± 0.18 and 0.48 ± 0.05 (Ab1) to 3.51 ± 0.13 and 0.76 ± 0.03 in the 30/60 one.

3.3. n-Alkanoic acids

Fatty acids are largely dominated by long chain saturated homologues in both soil sequences (more than 90% of total FAs) while unsaturated straight chain (mainly $C_{16:1}$ and $C_{18:1}$ homologues, data not shown) and branched homologues (odd numbered-carbon chain homologues from C_{13} to C_{19}) are less abundant (respectively less than 8% and 2% of total FAs). FA distributions range from C_6 to C_{34} and show strong EOP predominance with values higher than 3.4 and unimodal distributions mostly centered at C_{24} (Supplementary Fig. S2). In both pedosequences, EOP generally decrease with depth with values ranging from 4.11 ± 0.09 (Ab1) to 3.79 ± 0.08 (Ab4) along the 10/80 profile and from 4.31 ± 0.04 (Ab1) to 3.41 ± 0.02 (Ab4) along the 30/60 one (Fig. 5a,b).

379 The values of the FA C_{16+18} sat./unsat. ratio increase significantly from Ab1 (0.78 ± 0.06,
380 Fig. 5a) to Ab2 (3.82 ± 0.18) in the 10/80 sequence, then slightly increase from Ab2 to Ab4
381 (4.43 ± 0.37). In the 30/60 sequence, its values again increase significantly from Ab1 (1.32 ±
382 0.21, Fig. 5b) to Ab2 (6.57 ± 0.62), then remain similar in Ab3 (7.16 ± 0.72), and eventually
383 decrease to Ab4 (4.59 ± 0.33)
384 Index Grass values along the 10/80 sequence decrease from Ab1 (0.09 ± 0.03, Fig. 5a) to
385 Ab2 (0.03 ± 0.01), then remain similar from Ab2 to Ab4 (0.03 ± 0.00). Along the 30/60
386 sequence, this index slightly decreases with depth from 0.05 ± 0.01 (Ab1, Fig. 5b) to 0.03 ±
387 0.01 (Ab4), except in Ab3 which displays a large standard deviation overlapping other
388 horizon values. The Index Deciduous values along the 10/80 sequence are higher in Ab1
389 (0.36 ± 0.02) compared to Ab3 (0.42 ± 0.03), then decrease to Ab4 (0.36 ±0.01). In the 30/60
390 pedosequence, the values of the Index Deciduous values increase from Ab1 (0.29 ± 0.01) to
391 Ab2 (0.35 ± 0.01), then remain similar from Ab2 to Ab4 (0.36 ± 0.01).
392
393 *3.4. n-Aldehydes*
394 *n*-Aldehyde distributions range from C_{20} to C_{32} and show a strong EOP for both soil
395 sequences, with a unimodal distribution and a switch of C_{max} from C_{26} to C_{28} between Ab1
396 and Ab4, respectively (Supplementary Fig. S2). In the 10/80 sequence, the C_{26}/C_{28} ratio
397 decreases substantially from Ab1 (2.12 ± 0.30; Fig. 5a) to Ab2 (0.42 ± 0.02) then slightly
398 increases to Ab4 (0.50 ± 0.05), while it decreases along the whole 30/60 sequence especially
399 from Ab1 to Ab2, with values ranging from 2.40 ± 0.01 (Ab1; Fig. 5b) to 0.62 ± 0.03 (Ab4).
400
401 *3.5. Functionalised triterpenoids*

In both soil profiles, sitosterol is the most abundant functionalised triterpenoid in the Ab1 horizon (40 ± 3% in 10/80 and 35 ± 1% in 30/60; (Supplementary Fig. S3), while ursolic acid is the most abundant in the other three horizons (more than 40% in 10/80 and more than 28% in 30/60). In the 10/80 pedosequence, the relative abundance of ursolic acid significantly increases from Ab1 to Ab2, and its subsequent variation with depth is minor compared to this first increase (Fig. 6a). In the 30/60 sequence, the abundance of ursolic acid increases from Ab1 to Ab2, then decreases from Ab2 to Ab3 and eventually increases to Ab4 (Fig. 6b). Within 10/80 and 30/60 pedosequences, the sum of the abundances of betulin, betulinic acid, lupeol and lupenone (referred as *Betulaceae* markers) increases from Ab1 (1.7 ± 0.9% and 1.3 ± 0.4% of functionalised triterpenoids, respectively; Fig. 6a, b) to Ab3 (4.7 ± 0.8% and 5.0 ± 1.8%), and decreases from Ab3 to Ab4 (2.3 ± 0.4% and 1.5 ± 0.1%). In all samples, cholesterol accounted for less than 5% of functionalised triterpenoids. In the 10/80 sequence, the values of the sitosterol to stanol ratio decrease from Ab1 (8.56 ± 0.76; Fig. 6a) to Ab2 (4.52 ± 0.95) and then remain similar to Ab4 (4.70 ± 0.43). In the 30/60 sequences, the ratio overall decrease with depth, with values ranging from 7.93 ± 0.71 (Ab1; Fig. 6b) to 1.73 ± 0.22 (Ab4).

3.6. brGDGTs

Only 5-methyl brGDGTs were detected in the different samples from the two sequences, with a large predominance of acyclic compounds Ia and IIa, and to a lesser extent homologue IIIa (Supplementary Fig. S4). Along the 10/80 pedosequence, the reconstructed MAT derived from the different brGDGT calibrations display similar qualitative trends with a decrease from Ab1 to Ab2, and a progressive increase from Ab2 to Ab4 (Fig. 7a). MAT_{MBT} (Weijers et al., 2007) values decrease from Ab1 (2.3 ± 0.4 °C) to Ab2 (0.0 ± 0.4 °C), then increase to

Ab4 (2.4 ± 0.1 °C). $MAT_{MBT'}$ (Peterse et al., 2012) values decrease from Ab1 (6.3 ± 0.3 °C) to Ab2 (4.8 ± 0.3 °C), then increase to Ab4 (6.4 ± 0.1 °C). MAT_{mr} (De Jonge et al., 2014) values decrease from Ab1 (7.6 ± 0.7 °C) to Ab2 (3.1 ± 0.4 °C), then increase to Ab4 (6.4 ± 0.2 °C). MAT_{5Me} (De Jonge et al., 2014) values decrease from Ab1 (7.6 ± 0.7 °C) to Ab2 (6.1 ± 0.3 °C), then increase to Ab4 (9.1 ± 0.2 °C). Similarly, reconstructed MAT from the 30/60 sequence exhibit similar variation trends whatever the calibration used, with a more or less pronounced decrease from Ab1 to Ab2, followed by a slight increase from Ab2 to Ab3 and from Ab3 to Ab4 (Fig. 7b). MAT_{MBT} (Weijers et al., 2007) values decrease from Ab1 (2.3 ± 0.4 °C) to Ab2 (0.0 ± 0.4 °C), then increase to Ab4 (3.4 ± 0.1 °C). $MAT_{MBT'}$ (Peterse et al., 2012) values decrease from Ab1 (6.3 ± 0.3 °C) to Ab2 (4.8 ± 0.3 °C), then increase to Ab4 (6.9 ± 0.1 °C). MAT_{mr} (De Jonge et al., 2014) values decrease from Ab1 (5.2 ± 0.2 °C) to Ab2 (4.5 ± 0.2 °C), then increase to Ab4 (5.6 ± 0.4 °C). MAT_{5Me} (De Jonge et al., 2014) values decrease from Ab1 (8.0 ± 0.1 °C) to Ab2 (7.4 ± 0.1 °C), then increase to Ab4 (8.5 ± 0.3 °C). The different calibrations provide different absolute temperature values, the lowest MAT being reconstructed with the calibration by Weijers et al. (2007; MAT_{MBT}) along both the 10/80 and 30/60 sequences.

4. Discussion

4.1. Sources of organic matter in the tundra meadow palaeosols adjacent to ÎArte 6

4.1.1. Natural vs anthropogenic OM

The composition of the SOM derived from lipid indices and ratios in buried A horizons from both 10/80 and 30/60 sequences showed overall similar variations with depth (e.g., ratios/proxies based on *n*-alkanes; saturated fatty acids and *n*-aldehydes; functionalized triterpenoids; brGDGTs, Figs. 4–7, respectively). These geochemical similarities occur

450 despite the fact that they probably represent two different human and animal activity areas (a
451 campsite vs an animal congregating area), as suggested by the presence of artefacts and
452 micro-refuse (charcoal, ceramics, etc.) in the 30/60 sequence alone (Anderson et al., 2019).
453 This suggests that the anthropogenic impacts on the relative abundances of the different lipid
454 biomarkers were limited despite the contrasting occupation histories of the two
455 pedosequences, and that the environmental proxies derived from these lipid families can be
456 used for palaeoenvironmental reconstruction. This also implies that even though it was not
457 possible to stratigraphically link the horizons in the two distant soil profiles, the dates of their
458 buried A horizons are likely to be roughly correlated.
459
460 *4.1.2. Plant vs microbial OM*
461 The diversity of *n*-alkyl families found in SOM, the large predominance of their long-
462 chain homologues and their distinctive EOP (*n*-alkanoic acids, *n*-alkanols, *n*-aldehydes α,ω-
463 hydroxy alkanoic acid) or OEP (*n*-alkanes, *n*-alkan-2-ones) strongly suggest that lipids from
464 Î Arte 6 palaeosols mainly derive from plant material (Jansen and Wiesenberg, 2017;
465 Supplementary Fig. S2). Similarly, the high diversity of hydrocarbons and functionalized
466 triterpenoids, and the predominance of phytosterols (Supplementary Fig. S3) suggest a major
467 input of plant-derived OM in soils (Volkman, 2005). Nevertheless, the presence of OM
468 derived from microbial sources and activities to SOM cannot be excluded as microorganisms
469 (including mycorrhizal fungi) can produce long-chain *n*-alkyl compounds (Nguyen Tu et al.,
470 2011) and a non-negligible amount of certain functionalized triterpenoids to SOM
471 (Grandmougin-Ferjani et al., 1999). However, their contribution to SOM is generally
472 considered negligible compared to plant-derived straight chain *n*-alkyl lipids and triterpenoids
473 (Bai et al., 2009). Also, the presence at low abundance of branched and short chain fatty acids

474 (*iso* and *anteiso* homologues, C_{13} to C_{19}, data not shown), cholesterol as well as bacterial
475 brGDGTs in SOM suggest the occurrence, but limited, of microorganism-derived lipids in
476 palaeosols.
477 The occurrence of some post-depositional biodegradation of palaeovegetation-derived
478 lipids by soil microbial communities is suggested by the decrease with depth of the FA EOP
479 (Schäfer et al., 2016; Fig. 4), the sitosterol/sitostanol ratio (Gaskell and Eglinton, 1976; Fig.
480 6) and the increase in the FA C_{16+18} sat./unsat. ratio (Wiesenberg et al., 2015; Fig. 5), mainly
481 observed between Ab1 and Ab2. However, this microbial degradation of organic matter
482 seems limited, as the values of the FA C_{16+18} sat./unsat. ratio remain lower than 10 and
483 decreasing or similar values with depth from Ab2 to ab4 suggest OM preservation
484 (Wiesenberg et al., 2015).
485 The limited impact of microbial degradation is also suggested by the values of FA EOP,
486 which are higher or similar (for Ab4 from the 30/60 profile, EOP = 3.41 ± 0.06; Fig. 5) to the
487 values found by Schäfer et al. (2016) in the second topsoil under a deciduous litter (EOP =
488 3.46). In addition, the relatively high *n*-alkane OEP values found along both soil profiles (>
489 5), although far lower than fresh plant material analysed by Zech et al. (2009; OEP = 15.0 for
490 grass and herbs and OEP = 17.9 for deciduous trees), remain higher that the OEP values
491 analysed in the soil samples under grassland (OEP = 4.5) and deciduous forest (OEP = 5.0)
492 from the same study. Their increasing trend with depth support a low bacterial biodegradation
493 of plant wax-derived *n*-alkanes along the Ì^Arte 6 palaeosols (Zech et al., 2009). Also, the *n*-
494 alkane CPI values lower than 10 (Fig. 4) suggest some microbial degradation of the native
495 plant lipids, but, as their values remain much higher than 1, lipid degradation seems limited
496 (Cranwell, 1981). Moreover, one would expect the *n*-alkane CPI values to decrease with
497 depth, as microbial degradation should increase with time in environmental archives. The fact

498 that opposite trends were observed in both pedosequences strongly suggests that this
499 degradation was low, or at least that the source/processes responsible for this proxy
500 overprinted that of microbial reworking.
501
502 *4.1.3. Palaeovegetation vs modern root-derived plant lipids*
503 As living roots from modern plant cover were present throughout both soil profiles (Fig.
504 2), their contribution to the SOM lipid pool has to be assessed to disentangle their signature
505 from that of actual palaeovegetation-derived biomarkers (Jansen and Wiesenberg, 2017). The
506 OEP and CDI values of *n*-alkanes in the soil samples (Fig. 4) are in the range of those of
507 plant leaves analysed by Ronkainen et al. (2015) and lower than those of roots
508 (Supplementary Fig. S6), suggesting that the impact of root-derived *n*-alkanes from modern
509 plants on the SOM of the analysed palaeosols is low. Regarding the other lipids, the
510 comparison of fatty acid, α,ω-hydroxy alkanoic acid and α,ω-alkanedioic acid composition of
511 local plants (aerial and sub-surface parts) could not be carried out and is highly dependent on
512 the context (Mendez-Millan et al., 2011; Gocke et al., 2013).
513 Overall, the analysis of the different lipids suggests that SOM in Î‌Arte 6 meadow
514 palaeosols is mainly derived from above-ground plant material, probably incorporated during
515 the development of each A horizon. Although minor microbial and root-derived lipid inputs
516 to palaeosol OM is likely, their lipid signatures do not seem to have been overprinted by that
517 of aerial plant material. In addition, although some proxy trends suggest a possible early
518 degradation of certain lipids (sitosterol/sitostanol and saturated/unsaturated C_{16+18} FA ratios),
519 the absence of clear and shared trends between these proxies (*n*-alkane OEP, FA EOP)
520 suggest a relatively good preservation of the lipids throughout the pedosequences, most

probably facilitated by the local cold conditions (Zimov et al., 2006), which argue in favour of a fairly good representation of lipid signatures as palaeovegetation biomarkers.

4.2. Reconstruction of the local palaeovegetation during the occupation of ÎArte 6

Due to the incomplete pollen records from the soil monoliths taken from the sections of the archaeological excavation area and the lake sediment core (Panova, 2008; Anderson et al., 2019), the goal of this study was to use lipid biomarkers from buried soil OM to reconstruct the local palaeovegetation.

The high *n*-alkane OEP values of the oldest (Ab4; Fig. 4) palaeosols of ÎArte 6 meadow are closer to those of the fresh dwarf shrubs leaves analysed by Ronkainen et al. (2015; Supplementary Fig. S6; *Rubus chameamorous* and *Vaccinum uliginossum*) than to those of grasses (*Carex aqualitis* and *Eriophorum* sp.). The progressive decrease in *n*-alkane OEP values from the oldest to the youngest palaeosol towards intermediate values between those of shrubs and those of grasses suggests a decreasing contribution of shrub-derived *n*-alkanes to SOM. This trend might be the result of a growing contribution of grass-derived *n*-alkanes, as OEP values remained higher than those of fresh grasses analysed by Ronkainen et al. (2015, 6.0 for *Eriophorum*). The contribution of moss- and root-derived lipids is likely limited as the OEP values of SOM remain largely higher than theirs. Similarly, the high values of the *n*-alkane C_{31}/C_{27} and C_{33}/C_{27} ratios found in the oldest palaeosol of the 10/80 pedosequence (8.3 and 2.0, respectively; Fig. 4) are more comparable to those of the dwarf shrubs *E. nigrum* and *L. palustris* than any other plant species or part, and their decrease over time toward lower values higher up the sequence suggests a progressive and concomitant decrease of the shrub cover along with a increase in the grass cover. In addition, the CDI values encountered in the Ab3 and Ab4 palaeosols from the 10/80 pedosequence (2. 1 and

545 1.9, respectively; Fig. 4) are as low as those found in dwarf shrub leaves from Ronkainen et
546 al. (2015, CDI ≤ 2.1 for *B. nana*, *E. nigrum*, *L. palustris* and *V. uliginossum*), while the
547 higher CDI values of the youngest palaeosols tend towards CDI values encountered in
548 grasses, mosses and roots.

549 In our soil sequences, both OEP and CPI of *n*-alkanes increase with depth (Fig. 4), which
550 likely results from vegetation shifts rather than post-depositional degradation of the native
551 biomarkers. Indeed, the preferential degradation of *n*-alkanes occurring in environmental
552 archives is generally highlighted by a decrease in OEP and CPI with depth, even though such
553 a decrease can also result from palaeovegetation changes (Thomas et al., 2021). Altogether,
554 the trends of the above-mentioned *n*-alkane-based proxies (OEP, C_{31}/C_{27} and C_{33}/C_{27} ratios
555 and CDI) suggest a gradual decrease in the abundance of dwarf shrub species relative to
556 grasses over time.

557 The overall increase with time in the fatty acid-derived Index Grass along with the
558 decrease in the Index Deciduous (Schäfer et al., 2016) in both pedosequences also suggest a
559 shift in the palaeovegetation with a decreasing shrub cover for the benefit of grasses (Fig. 5).
560 The increase in the aldehyde C_{26}/C_{28} ratio values observed in the two soil sequences from the
561 bottom palaeosol to the top one might also indicate an increased contribution in grass lipids
562 to SOM over time (Fig. 5), as grasses and herbs can contain higher proportions of C_{26}
563 compared to shrubs and trees, richer in C_{28} and longer homologues (van Bergen et al., 1997).

564 The overall decrease in ursolic acid abundance in the two pedosequences from the oldest
565 palaeosol to the youngest (Fig. 6) could also be attributed to a decreasing contribution of
566 shrubs to palaeovegetation cover (Fisher et al., 2003). Finally, a decreasing trend in shrub
567 cover over time was also observed in the pollen diagram from the Î‍Arte 6 on-site monolith
568 (Supplementary Mat. 8 in Anderson et al., 2019). As mosses can display significantly higher

569 *n*-alkane C_{23}/C_{25} and C_{23}/C_{27} ratio values compared to other plant species (Ronkainen et al.,
570 2015; Fig. 4; Supplementary Fig. S6), the increasing values of these proxies from the bottom
571 to the top of our pedosequences argue for an increase in the contribution of mosses to
572 palaeovegetation over time. However, as the values of these ratios are low in our soils
573 compared to those of fresh mosses, the contribution of mosses to the palaeovegetation of the
574 meadow studied might be limited in comparison to that of shrubs and grasses.
575 Altogether, these results suggest that the dwarf shrub species dominated the
576 palaeovegetation at ÎArte 6 when the Ab4 palaeosol developed, and then that the plant cover
577 evolved toward an increasing and higher contribution of grasses and mosses.
578 The concomitant occurrence of betulin, betulinic acid, lupeol and lupenone in
579 environmental and archaeological samples has been used as an indicator for the presence of
580 species from the *Betulaceae* family, which is dominated by shrubs and trees (Colombini and
581 Modugno, 2009). Indeed, these lipids are found in high abundance in different birch
582 subspecies compared to subspecies such as *Alnus*, *Corylus* and *Carpinus* and other families
583 such as *Salicaceae* or *Ericaceae* (Supplementary materialin Diefendorf et al., 2012). In the
584 present study, the sum of the relative abundance of betulin, betulinic acid, lupeol and
585 lupenone followed a trend different to the one of *n*-alkane proxies reflecting the overall shrub
586 contribution (i.e. *n*-alkane-derived OEP, C_{31}/C_{27} and C_{33}/C_{27} ratios), suggesting that these
587 compounds could record the specific variations of *Betulaceae* species. The fact that the
588 variations of this specific *Betulaceae* proxy are not visible in the trends of more general shrub
589 proxies suggests that the contribution of *Betulaceae* species to the global shrub lipid signature
590 was probably low. This is in accordance with the current local predominance of shrubs like
591 *Vaccinium* sp., *Rubus* sp. or *Salix* sp. (Supplementary Table S1), although the balance in
592 shrub species distribution probably changed over time. The highest abundance of *Betulaceae*

markers recorded in the third and the second palaeosols (Ab3 and Ab2; Fig. 6) could correspond to the high peak of *Betula nana* pollen displayed at 60 and 80 cm depth in the ÎArte 6 soil monolith (Supplementary Fig. S7a), all the more as the other shrub-derived pollen (*Alnus*, *Salix* and different *Ericaceae*) did not show such variation.

4.3. Regional palaeoclimate reconstruction

Several global calibrations based on brGDGT distribution in soils (Weijers et al., 2007; Peterse et al., 2012; De Jonge et al., 2014) were applied to reconstruct mean annual temperature (MAT). The most recent brGDGT calibrations (e.g., De Jonge et al., 2014; Véquaud et al., 2022) rely on improved analytical methods allowing the separation of 5- and 6-methyl brGDGTs. The exclusion of 6-methyl brGDGTs was shown to improve the accuracy of MAT reconstructions compared to previous global calibrations where the two types of homologues were not separated (cf. De Jonge et al., 2014). Nevertheless, even though 6-methyl brGDGTs are present in most soil samples discussed in the literature, including those previously analysed in our laboratory (e.g., Huguet et al., 2019), they are sometimes not detected (e.g., in 17 out of 239 soils reported by De Jonge et al., 2014), as was the case in the samples from the palaeosol sequences at ÎArte 6. Therefore, in the present case, whatever the calibration, the MAT reconstructions are based on 5-methyl brGDGTs (Fig. 7).

The tentative MAT reconstructions based on the different calibrations showed similar trends from the oldest to youngest palaeosols in the ÎArte 6 meadow sequences (Fig. 7) and followed roughly the regional temperature anomalies reconstructed by Briffa et al. (2013) based on high-resolution dendroclimatological data (see Fig. 11 in Anderson et al., 2019). Similarly to brGDGTs (Fig. 7), in the 10/80 pedosequence, the variations of soil magnetic

susceptibility, a palaeoclimate proxy often used in LPS contexts (Kravchinsky et al., 2008; Zeng and Yang, 2019), suggests that regional temperatures were slightly higher in the oldest and the youngest palaeosols than in the second and the third palaeosols developing in the ÎArte 6 meadow (Fig. 7). The trends observed in the 10/80 palaeosol sequence are also supported by pollen analysis in a regional record from a lake located a few kilometres southwest of ÎArte 6 (Lake Three; Anderson et al., 2019), where a decrease in grasses relative to shrubs occurred around 800 CE. This was interpreted as a result of an increase in air temperature (Supplementary Fig. S7b), which can be correlated to the transition between the Ab2 palaeosol (718–916 CE) and the Ab1 (838–1037 CE), and the corresponding MAT variations (Fig. 7).

Overall, the trends in palaeoclimate recorded by brGDGTs in both pedosequences suggest that a decrease in air temperature occurred between the 6th and 7th centuries CE, followed by warmer temperatures between the 8th and the 10th centuries CE (Fig. 7).

However, whatever the calibration, the absolute values of MAT inferred from brGDGTs in the palaeosols were too high compared to the modern MAT measured at the Mare-Sale weather station, which are ca. –8 °C (150 km NW from the site, Vikhamar-Schuler et al., 2010). These differences between MAT estimates and actual temperatures could be the result of; (a) a lack of brGDGT-based calibrations for high latitude soil environments, (b) the impacts of various vegetation assemblages, suggested by other lipid biomarkers, on the calibrations of brGDGT-based temperature proxies (Liang et al., 2019), (c) a minor contribution of brGDGTs derived from rhizomicrobial association (Huguet et al., 2012; but see discussion in Section 4.1), and/or (d) brGDGT distribution being more representative of summer environmental conditions, when bacteria are more active (Huguet et al., 2013). Bearing this in mind, when a high latitude lacustrine calibration (Foster et al., 2016) allowing

641 the reconstruction of mean summer temperature (MST) is applied to our soils, the
642 reconstructed temperatures (increasing with depth from 4.4 °C to 8.9 °C in the 10/80
643 sequence, data not shown) fit better with the actual local summer temperatures (ca. 7 °C at
644 Mare-Sale, Vikhamar-Schuler et al., 2010). This stresses the need for the development of
645 regional brGDGT calibrations based on modern datasets from comparable, high-latitude
646 environments, and for the combination of brGDGTs with other temperature proxies, such as
647 those based on chironomids (Langdon et al., 2011). However, the current results highlight the
648 potential of GDGT-based proxies to provide information on past regional temperature
649 variations in loess-palaeosol sequences, which has significant implications for palaeoclimate
650 reconstructions and archaeological studies elsewhere.
651
652 *4.4. ÎArte 6 palaeoreconstruction and history*
653 Finally, the different proxies used in this study show a good agreement between the
654 molecular signatures in the palaeosols and the regional palaeoenvironmental reconstructions
655 (Panova et al., 2008; Briffa et al., 2013; Anderson et al., 2019). During the time period
656 covered by the ÎArte 6 meadow LPS, both the local lipid and pollen records show an increase
657 in grasses relative to shrubs (Figs. 4–6). This vegetation shift might be due to the cooling
658 climate observed until the 9th century (Fig. 7; Schubert et al., 2019), but it may also have been
659 promoted by the gradual intensification of human and reindeer presence at the site (Anderson
660 et al., 2019). Although they may originally have used the shrubs of the ÎArte 6 headland as
661 hunting hides (Anderson et al., 2019), the presence of willow and birch charcoal in buried
662 hearths found at the site and in the palaeosol sequences adjacent at the site (especially at
663 30/60), and the trends observed for specific pentacyclic triterpenoids as potential dwarf birch
664 biomarkers, indicate that the shrub cover was harvested for firewood. At the same time, the

665 presence of congregating reindeer at different periods testified by the faecal lipid biomarker
666 data (Anderson et al., 2019) may have decreased the shrub cover by repetitive trampling and
667 selective grazing on dwarf shrubs, and by promoting grass growth over shrubs via urine and
668 faeces fertilization as it is observed in modern contexts (Olofsson, 2006; Skarin et al., 2020).
669 The late increase in air temperature inferred from brGDGTs (Fig. 7) would have been
670 expected to promote shrubification in a tundra environment (Forbes et al., 2010). As an
671 opposite trend was observed, this suggests that the effects of the impacts of reindeer activity
672 at the site on the local vegetation cover, and especially shrubs, were most probably
673 predominant over of the possible positive impacts of climate on the promotion of shrub
674 species (Fig. 8).
675

676 **5. Conclusions**

677 In this study aiming to reconstruct the palaeoenvironment of a Siberian archaeological site,
678 the similar lipid signatures of two distinct palaeosol profiles containing a dominance of plant-
679 derived lipids (long-chain *n*-alkyl compounds, phytosterols and pentacyclic triterpenoids)
680 showed that human and animal activities had a greater impact on the local vegetation than
681 regional climate change. This multi-proxy study included a rigorous evaluation of the plant-
682 derived lipid preservation in the soil sequences studied. Although post-depositional bacterial
683 degradation of plant lipids did occur, the values and trends with depth of the
684 sitosterol/sitostanol ratio, the FA C_{16+18} sat./unsat. ratio, FA EOP and *n*-alkane OEP and CPI
685 proxies suggested that this was limited. *n*-Alkane OEP and CDI proxy values also argue in
686 favour of a limited impact of modern roots on the SOM, implying that SOM lipid signatures
687 were representative of the palaeovegetation at the site.

The values and trends of different lipid-based palaeovegetation proxies (*n*-alkane CDI, OEP, C_{23}/C_{25} and C_{23}/C_{27}, C_{31}/C_{27} and C_{33}/C_{27} ratios, FA Index and *n*-aldehyde C_{26}/C_{28} ratio) from the oldest to the youngest palaeosols support the shift from an early predominance of dwarf shrub species to an increasing contribution of grasses and mosses, as also suggested by pollen analysis and the modern vegetation cover, although the different trends of some triterpene compounds (betulin, betulinic acid, lupeol and lupenone) imply independent temporal variation of *Betulaceae* shrub.

The trends in palaeoclimate recorded by brGDGT-based MAT reconstructions suggest that a decrease in air temperature occurred between the 6th and 7th centuries CE, followed by warmer temperatures between the 8th and 10th centuries CE. Temperature increases in the Arctic are normally associated with the promotion of shrub species over grasses, but in this case, the palaeovegetation proxies suggest the opposite. This bifurcation of local vegetation and regional climate trends is most likely to be the result of the occupation of the site by reindeer herders and their herds and their impacts on local vegetation, including grazing, trampling, the harvesting of shrubs for firewood, and the input of dung.

This study demonstrates that palaeovegetation and palaeoclimate reconstructions based on multi-proxy lipid biomarker analysis, when applied to archaeological contexts, are an important complement to routine archaeological and palynological studies, as they enable the distinction between climatic and anthropogenic impacts on local vegetation. Understanding past impacts of human occupation and reindeer herding on Arctic vegetation will facilitate the management of Arctic ecosystems in the wake of ongoing climate change.

Acknowledgments

This study was funded by the ESRC ES/ M011054/1 "JPI Climate: Social-Ecological Transformations: HUMan-ANimal Relations Under Climate Change in NORthern Eurasia" held at the University of Aberdeen, within the Nordforsk network HUMANOR at the University of Lapland (Decision #291581), by the European Research Council (ERC) Advanced Grant 295458 "Arctic Domus" and by the Leverhulme Trust (Grant RPG-2019-258)

We thank Julia Kremkova, Andreĭ Plekhanov, Konstantin Oshchepekov and their team for their help with our fieldwork. We thank Organic Geochemistry co-Editor-in-Chief John Volkman, Associate Editors Phil Meyers and Klaas Nierop, and three reviewers for their constructive comments and suggestions. We are also grateful for helpful comments from Sylvie Derenne, and for modern plant cover data and HUMANOR project leadership by Bruce Forbes.

Declaration of interest

Declarations of interest: None.

Associate Editor–**Klaas Nierop**

References

Anderson, D.G., Ineshin, E.M., Kulagina, N.V., Lavento, M., Vinkovskaya, O.P., 2014. Landscape agency and Evenki-Iakut reindeer husbandry along the Zhuia River, eastern Siberia. Human Ecology 42, 249–266.

735 Anderson, D.G., Harrault, L., Milek, K.B., Forbes, B.C., Kuoppamaa, M., Plekhanov, A. V.,
736 2019. Animal domestication in the high Arctic: Hunting and holding reindeer on the
737 ÎAmal peninsula, northwest Siberia. Journal of Anthropological Archaeology 55.
738 doi:10.1016/j.jaa.2019.101079
739 Andreev, A., Tarasov, P., Schwamborn, G., Ilyashuk, B., Ilyashuk, E., Bobrov, A., Klimanov,
740 V., Rachold, V., Hubberten, H.-W., 2004. Holocene paleoenvironmental records from
741 Nikolay Lake, Lena River Delta, Arctic Russia. Palaeogeography, Palaeoclimatology,
742 Palaeoecology 209, 197–217.
743 Bai, Y., Fang, X., Nie, J., Wang, Y., Wu, F., 2009. A preliminary reconstruction of the
744 paleoecological and paleoclimatic history of the Chinese Loess Plateau from the
745 application of biomarkers. Palaeogeography, Palaeoclimatology, Palaeoecology 271,
746 161–169.
747 Briffa, K.R., Melvin, T.M., Osborn, T.J., Hantemirov, R.M., Kirdyanov, A.V., Mazepa, V.S.,
748 Shiyatov, S.G., Esper, J., 2013. Reassessing the evidence for tree-growth and inferred
749 temperature change during the Common Era in Yamalia, northwest Siberia. Quaternary
750 Science Reviews 72, 83–107.
751 Colombini, M.P., Modugno, F., 2009. Organic Mass Spectrometry in Art and Archaeology.
752 John Wiley and Sons, Chichester, UK. doi:10.1002/9780470741917
753 Cranwell, P.A., 1981. Diagenesis of free and bound lipids in terrestrial detritus deposited in a
754 lacustrine sediment. Organic Geochemistry 3, 79–89.
755 Davis, M. B., 2000. Palynology after Y2K—Understanding the source area of pollen in
756 sediments. Annual Review of Earth and Planetary Sciences 28, 1–18.
757 De Jonge, C., Hopmans, E.C., Zell, C.I., Kim, J.-H., Schouten, S., Sinninghe Damsté, J.S.,
758 2014. Occurrence and abundance of 6-methyl branched glycerol dialkyl glycerol

759 tetraethers in soils: Implications for palaeoclimate reconstruction. Geochimica et
760 Cosmochimica Acta 141, 97–112.
761 Diefendorf, A.F., Freeman, K.H., Wing, S.L., 2012. Distribution and carbon isotope patterns
762 of diterpenoids and triterpenoids in modern temperate C3 trees and their geochemical
763 significance. Geochimica et Cosmochimica Acta 85, 342–356.
764 Fisher, E., Oldfield, F., Wake, R., Boyle, J., Appleby, P., Wolff, G.A., 2003. Molecular
765 marker records of land use change. Organic Geochemistry 34, 105–119.
766 Forbes, B.C., Fauria, M.M., Zetterberg, P., 2010. Russian Arctic warming and 'greening' are
767 closely tracked by tundra shrub willows. Global Change Biology 16, 1542–1554.
768 Forbes, B.C., Kumpula, T., Meschtyb, N., Laptander, R., MacIas-Fauria, M., Zetterberg, P.,
769 Verdonen, M., Skarin, A., Kim, K.Y., Boisvert, L.N., Stroeve, J.C., Bartsch, A., 2016.
770 Sea ice, rain-on-snow and tundra reindeer nomadism in Arctic Russia. Biology Letters
771 12, 20160466.
772 Foster, L.C., Pearson, E.J., Juggins, S., Hodgson, D.A., Saunders, K.M., Verleyen, E.,
773 Roberts, S.J., 2016. Development of a regional glycerol dialkyl glycerol tetraether
774 (GDGT)–temperature calibration for Antarctic and sub-Antarctic lakes. Earth and
775 Planetary Science Letters 433, 370–379.
776 Gaskell, S.J., Eglinton, G., 1976. Sterols of a contemporary lacustrine sediment. Geochimica
777 et Cosmochimica Acta 40, 1221–1228.
778 Gocke, M., Kuzyakov, Y., Wiesenberg, G.L.B., 2013. Differentiation of plant derived
779 organic matter in soil, loess and rhizoliths based on *n*-alkane molecular proxies.
780 Biogeochemistry 112, 23–40.
781 Grandmougin-Ferjani, A., Dalpé, Y., Hartmann, M.-A., Laruelle, F., Sancholle, M., 1999.
782 Sterol distribution in arbuscular mycorrhizal fungi. Phytochemistry 50, 1027–1031.

783 Harrault, L., Milek, K., Jardé, E., Jeanneau, L., Derrien, M., Anderson, D.G., 2019. Faecal
784 biomarkers can distinguish specific mammalian species in modern and past
785 environments. PLoS ONE 14. doi:10.1371/journal.pone.0211119
786 Hjulström, B., Isaksson, S., 2009. Identification of activity area signatures in a reconstructed
787 Iron Age house by combining element and lipid analyses of sediments. Journal of
788 Archaeological Science 36, 174–183.
789 Huguet, A., Wiesenberg, G.L.B., Gocke, M., Fosse, C., Derenne, S., 2012. Branched
790 tetraether membrane lipids associated with rhizoliths in loess: Rhizomicrobial
791 overprinting of initial biomarker record. Organic Geochemistry 43, 12–19.
792 Huguet, A., Fosse, C., Laggoun-Défarge, F., Delarue, F., Derenne, S., 2013. Effects of a
793 short-term experimental microclimate warming on the abundance and distribution of
794 branched GDGTs in a French peatland. Geochimica et Cosmochimica Acta 105, 294–
795 315.
796 Huguet, A., Coffinet, S., Roussel, A., Gayraud, F., Anquetil, C., Bergonzini, L., Bonanomi,
797 G., Williamson, D., Majule, A., Derenne, S., 2019. Evaluation of 3-hydroxy fatty acids
798 as a pH and temperature proxy in soils from temperate and tropical altitudinal gradients.
799 Organic Geochemistry 129, 1–13.
800 Jansen, B., Nierop, K.G.J., Tonneijck, F.H., van der Wielen, F.W.M., Verstraten, J.M., 2007.
801 Can isoprenoids in leaves and roots of plants serve as biomarkers for past vegetation
802 changes? A case study from the Ecuadorian Andes. Plant and Soil 291, 181–198.
803 Jansen, B., Wiesenberg, G.L.B., 2017. Opportunities and limitations related to the application
804 of plant-derived lipid molecular proxies in soil science. Soil 3, 211–234.

805 Jordanova, N., Jordanova, D., Mokreva, A., Ishlyamski, D., Georgieva, B., 2019. Temporal
806 changes in magnetic signal of burnt soils – A compelling three years pilot study. Science
807 of the Total Environment 669, 729–738.
808 Kravchinsky, V.A., Zykina, V.S., Zykin, V.S., 2008. Magnetic indicator of global
809 paleoclimate cycles in Siberian loess–paleosol sequences. Earth and Planetary Science
810 Letters 265, 498–514.
811 Langdon, P.G., Caseldine, C.J., Croudace, I.W., Jarvis, S., Wastegård, S., Crowford, T.C.,
812 2011. A chironomid-based reconstruction of summer temperatures in NW Iceland since
813 AD 1650. Quaternary Research 75, 451–460.
814 Mendez-Millan, M., Dignac, M.-F., Rumpel, C., Derenne, S., 2011. Can cutin and suberin
815 biomarkers be used to trace shoot and root-derived organic matter? A molecular and
816 isotopic approach. Biogeochemistry 106, 23–38.
817 Modugno, F., Ribechini, E., Colombini, M.P., 2006. Chemical study of triterpenoid resinous
818 materials in archaeological findings by means of direct exposure electron ionisation mass
819 spectrometry and gas chromatography/mass spectrometry. Rapid Communications in
820 Mass Spectrometry 20, 1787–1800.
821 Müller, S., Tarasov, P.E., Andreev, A.A., Diekmann, B., 2009. Late Glacial to Holocene
822 environments in the present-day coldest region of the Northern Hemisphere inferred
823 from a pollen record of Lake Billyakh, Verkhoyansk Mts, NE Siberia. Climate of the
824 Past 5, 73–84.
825 Nguyen Tu, T.T., Egasse, C., Zeller, B., Bardoux, G., Biron, P., Ponge, J.F., David, B.,
826 Derenne, S., 2011. Early degradation of plant alkanes in soils: A litterbag experiment
827 using ^{13}C-labelled leaves. Soil Biology and Biochemistry 43, 2222–2228.

828 Niemeyer, B., Klemm, J., Pestryakova, L.A., Herzschuh, U., 2015. Relative pollen
829 productivity estimates for common taxa of the northern Siberian Arctic. Review of
830 Palaeobotany and Palynology 221, 71–82.
831 Nomokonova, T., Losey, R.J., Plekhanov, A. V., McIntyre, H.J., 2018. Iarte VI and late
832 Holocene reindeer remains from the Iamal Peninsula of Arctic Siberia. Arctic
833 Anthropology 55, 56–75.
834 Olofsson, J., 2006. Short- and long-term effects of changes in reindeer grazing pressure on
835 tundra heath vegetation. Journal of Ecology 94, 431–440.
836 Panova, N.K., 2008. Rekonstruk͡tsii͡a paleorastitel'nosti gorodishcha I͡Arte 6 na poluostrove
837 I͡Amal (po dannym sporovo-pyl't͡sevogo analiza). In: Kosintsev, P.A. (Ed.), Fauny i
838 Flory Severnoĭ Evrazii v Pozdnem Kaĭnozoe: Sb. Nauch. Trudov. TsIRK Rifei.
839 Ekaterinburg, pp. 244–248.
840 Peterse, F., van der Meer, J., Schouten, S., Weijers, J.W.H., Fierer, N., Jackson, R.B., Kim,
841 J.H., Sinninghe Damsté, J.S., 2012. Revised calibration of the MBT-CBT
842 paleotemperature proxy based on branched tetraether membrane lipids in surface soils.
843 Geochimica et Cosmochimica Acta 96, 215–229.
844 Plekhanov, A.V, 2014. I͡Arte 6 – srednevekovoe «gorodishche» na r. I͡Uribeĭ (p-ov I͡Amal).
845 Katalog kollekt͡siĭ. Ярте 6 – средневековое «городище» на р. Юрибей (п-ов Ямал).
846 Каталог коллекций. Delovai͡a pressa, Ekaterinburg.
847 Rees-Owen, R.L., Gill, F.L., Newton, R.J., Ivanović, R.F., Francis, J.E., Riding, J.B., Vane,
848 C.H., Lopes dos Santos, R.A., 2018. The last forests on Antarctica: Reconstructing flora
849 and temperature from the Neogene Sirius Group, Transantarctic Mountains. Organic
850 Geochemistry 118, 4–14.

851 Ritchie, J.C., 1995. Current trends in studies of long-term plant community dynamics. New
852 Phytologist 130, 469–494.
853 Romero-Sarmiento, M.-F., Riboulleau, A., Vecoli, M., Laggoun-Défarge, F., Versteegh,
854 G.J.M., 2011. Aliphatic and aromatic biomarkers from Carboniferous coal deposits at
855 Dunbar (East Lothian, Scotland): Palaeobotanical and palaeoenvironmental significance.
856 Palaeogeography, Palaeoclimatology, Palaeoecology 309, 309–326.
857 Ronkainen, T., Väliranta, M., McClymont, E., Biasi, C., Salonen, S., Fontana, S., Tuittila,
858 E.S., 2015. A combined biogeochemical and palaeobotanical approach to study
859 permafrost environments and past dynamics. Journal of Quaternary Science 30, 189–200.
860 Schäfer, I.K., Lanny, V., Franke, J., Eglinton, T.I., Zech, M., Vysloužilová, B., Zech, R.,
861 2016. Leaf waxes in litter and topsoils along a European transect. Soil 2, 551–564.
862 Schubert, M., Marcussen, T., Meseguer, A.S., Fjellheim, S., 2019. The grass subfamily
863 *Pooideae*: Cretaceous–Palaeocene origin and climate-driven Cenozoic diversification.
864 Global Ecology and Biogeography 28, 1168–1182.
865 Simoneit, B.R.T., 2005. A review of current applications of mass spectrometry for
866 biomarker/molecular tracer elucidations. Mass Spectrometry Reviews 24, 719–765.
867 Skarin, A., Verdonen, M., Kumpula, T., Macias-Fauria, M., Alam, M., Kerby, J., Forbes,
868 B.C., 2020. Reindeer use of low Arctic tundra correlates with landscape structure.
869 Environmental Research Letters 15, 115012.
870 Tarasov, P.E., Müller, S., Zech, M., Andreeva, D., Diekmann, B., Leipe, C., 2013. Last
871 glacial vegetation reconstructions in the extreme-continental eastern Asia: Potentials of
872 pollen and *n*-alkane biomarker analyses. Quaternary International 290–291, 253–263.
873 Thomas, C.L., Jansen, B., van Loon, E.E., Wiesenberg, G.L.B., 2021. Transformation of *n*-
874 alkanes from plant to soil: a review. Soil 7, 785–809.

875 Van Bergen, P.F., Bull, I.D., Poulton, P.R., Evershed, R.P., 1997. Organic geochemical
876 studies of soils from the Rothamsted Classical Experiments - I. Total lipid extracts,
877 solvent insoluble residues and humic acids from Broadbalk Wilderness. Organic
878 Geochemistry 26, 117–135.
879 Véquaud, P., Thibault, A., Derenne, S., Anquetil, C., Collin, S., Contreras, S., Nottingham,
880 A.T., Sabatier, P., Werne, J.P., Huguet, A., 2022. FROG: A global machine-learning
881 temperature calibration for branched GDGTs in soils and peats. Geochimica et
882 Cosmochimica Acta 318, 468–494.
883 Verdonen, M., Berner, L.T., Forbes, B.C., Kumpula, T., 2020. Periglacial vegetation
884 dynamics in Arctic Russia: decadal analysis of tundra regeneration on landslides with
885 time series satellite imagery. Environmental Research Letters 15, 105020.
886 Vikhamar-Schuler, D., Hanssen-Bauer, I., Førland, E., 2010. Long-term climate trends of the
887 Yamalo-Nenets AO, Russia. Norwegian Meteorological Institute Report 8.
888 https://www.met.no/publikasjoner/met-report/met-report-2010
889 Volkman, J.K., 2005. Sterols and other triterpenoids: source specificity and evolution of
890 biosynthetic pathways. Organic Geochemistry 36, 139–159.
891 Weijers, J.W.H., Schouten, S., van den Donker, J.C., Hopmans, E.C., Sinninghe Damsté, J.S.,
892 2007. Environmental controls on bacterial tetraether membrane lipid distribution in soils.
893 Geochimica et Cosmochimica Acta 71, 703–713.
894 Wiesenberg, G.L.B., Andreeva, D.B., Chimitdorgieva, G.D., Erbajeva, M.A., Zech, W.,
895 2015. Reconstruction of environmental changes during the late glacial and Holocene
896 reflected in a soil-sedimentary sequence from the lower Selenga River valley, Lake
897 Baikal region, Siberia, assessed by lipid molecular proxies. Quaternary International 365,
898 190–202.

Zech, M., Rass, S., Buggle, B., Löscher, M., Zöller, L., 2012. Reconstruction of the late Quaternary paleoenvironments of the Nussloch loess paleosol sequence, Germany, using *n*-alkane biomarkers. Quaternary Research 78, 226–235.

Zech, M., Buggle, B., Leiber, K., Marković, S., Glaser, B., Hambach, U., Huwe, B., Stevens, T., Sümegi, P., Wiesenberg, G., Zöller, L., 2009. Reconstructing Quaternary vegetation history in the Carpathian Basin, SE-Europe, using *n*-alkane biomarkers as molecular fossils: Problems and possible solutions, potential and limitations. Quaternary Science Journal 58, 148–155.

Zeng, F., Yang, H., 2019. Temperature changes reconstructed from branched GDGTs on the central Loess Plateau during the past 130–5 ka. Quaternary International 503, 3–9.

Zimov, S.A., Davydov, S.P., Zimova, G.M., Davydova, A.I., Schuur, E.A.G., Dutta, K., Chapin, I.S., 2006. Permafrost carbon: Stock and decomposability of a globally significant carbon pool. Geophysical Research Letters 33, L20502.

Figure captions

Fig. 1. Location of: (a) the ÎAmal Peninsula; (b) the ÎArte complex; (c) ÎArte 6 elevation model, including the locations of the loess-palaeosol sequences in test pits 10/80 and 30/60, the location of the different excavations conducted, modern vegetation community analysis (Bruce Forbes, 1996, quadrat numbers as in Supplementary Table S1) and the location of the soil monolith analysed for pollen (Anderson et al., 2019).

Fig. 2. Pedosequence description of soil test pits located at 10/80 and 30/60 (Fig. 1). Soil horizon notation corresponds to FAO (2006), A for buried palaeosol and C for wind-deposited

sediment. Soil sampling for lipid analyses is described in detail in the Material and Method section. Radiocarbon dates are from Anderson et al. (2019).

Fig. 3. Total ion current (TIC) chromatograms of the: (a) apolar and (b) polar fractions of a soil methodological replicate from the Ab4 horizon of sequence 30/60. C# displays the length of the *n*-alkyl chain. Compound names, formulae and other structural and spectral details can be found in Supplementary Table S3.

Fig. 4. Depth variations of *n*-alkane-based proxies in palaeosols from sequences: (a) 10/80 and (b) 30/60. Proxy calculations are detailed in the Materials and methods section.

Fig. 5. Depth variations of fatty acid-based proxies and the C_{26}/C_{28} *n*-aldehyde ratio in palaeosols from sequences: (a) 10/80 and (b) 30/60. Proxy calculations are detailed in the Materials and method section.

Fig. 6. Depth variations of ursolic acid, suggested *Betulaceae* biomarkers (sum of betulin, betulinic acid, lupeol and lupenone) and sitosterol/sitostanol ratio in palaeosols from sequences (a) 10/80 and (b) 30/60.

Fig. 7. Depth variations of reconstructed mean annual temperature (MAT) based on brGDGT-derived calibrations by Weijers et al. (2007; MATMBT), Peterse et al. (2012; MATMBT′) and De Jonge et al. (2014; MAT5Me and MATmr) in palaeosols from sequences: (a) 10/80 and (b) 30/60. The different brGDGT calibrations are detailed in the Materials and methods section.

947 **Fig. 8**. Schematic representation of the evolution of human-animal-environment relationship
948 and palaeoenvironmental conditions at ÎArte 6.

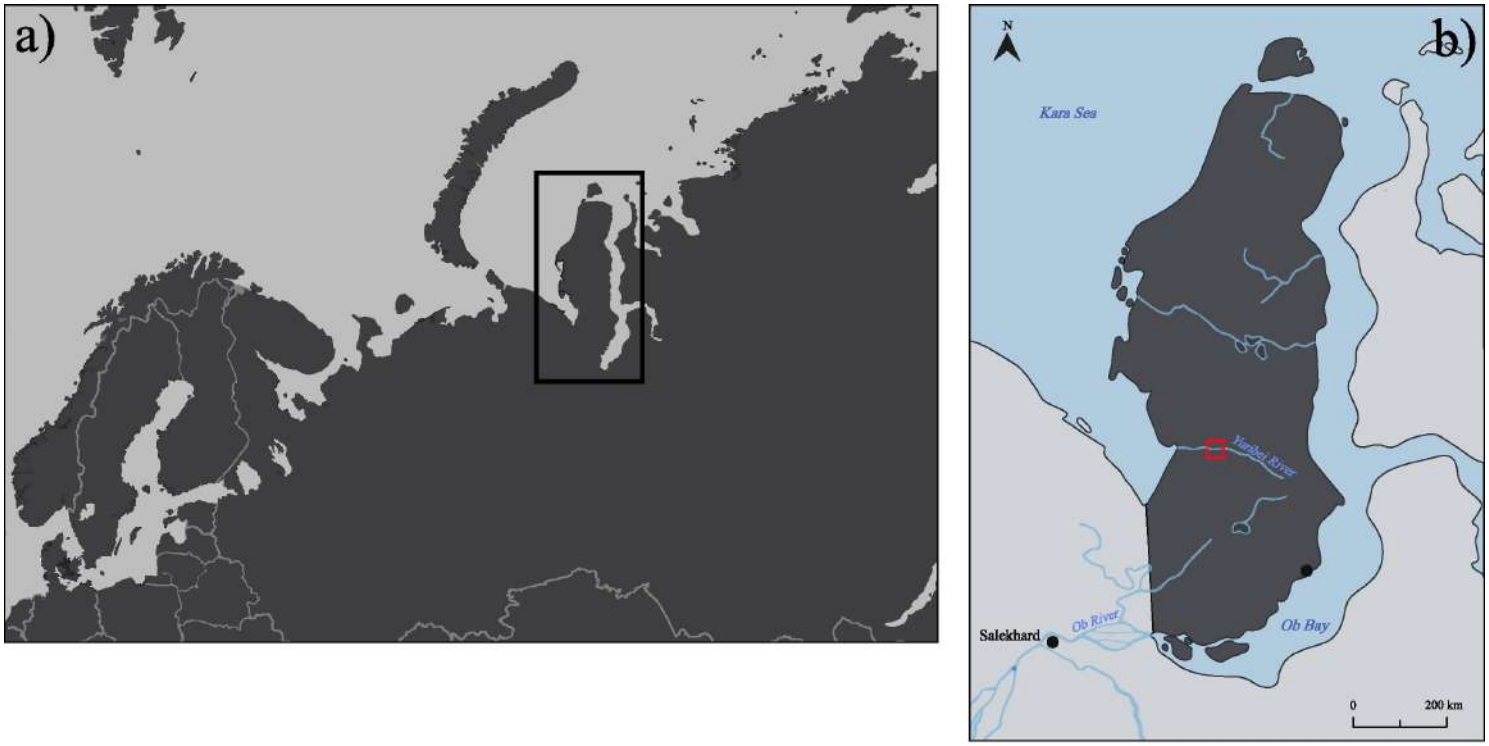
a)
b)
N
Kara Sea
Yarbeyi River
Salekhard
Ob River
Ob Bay
0
200 km

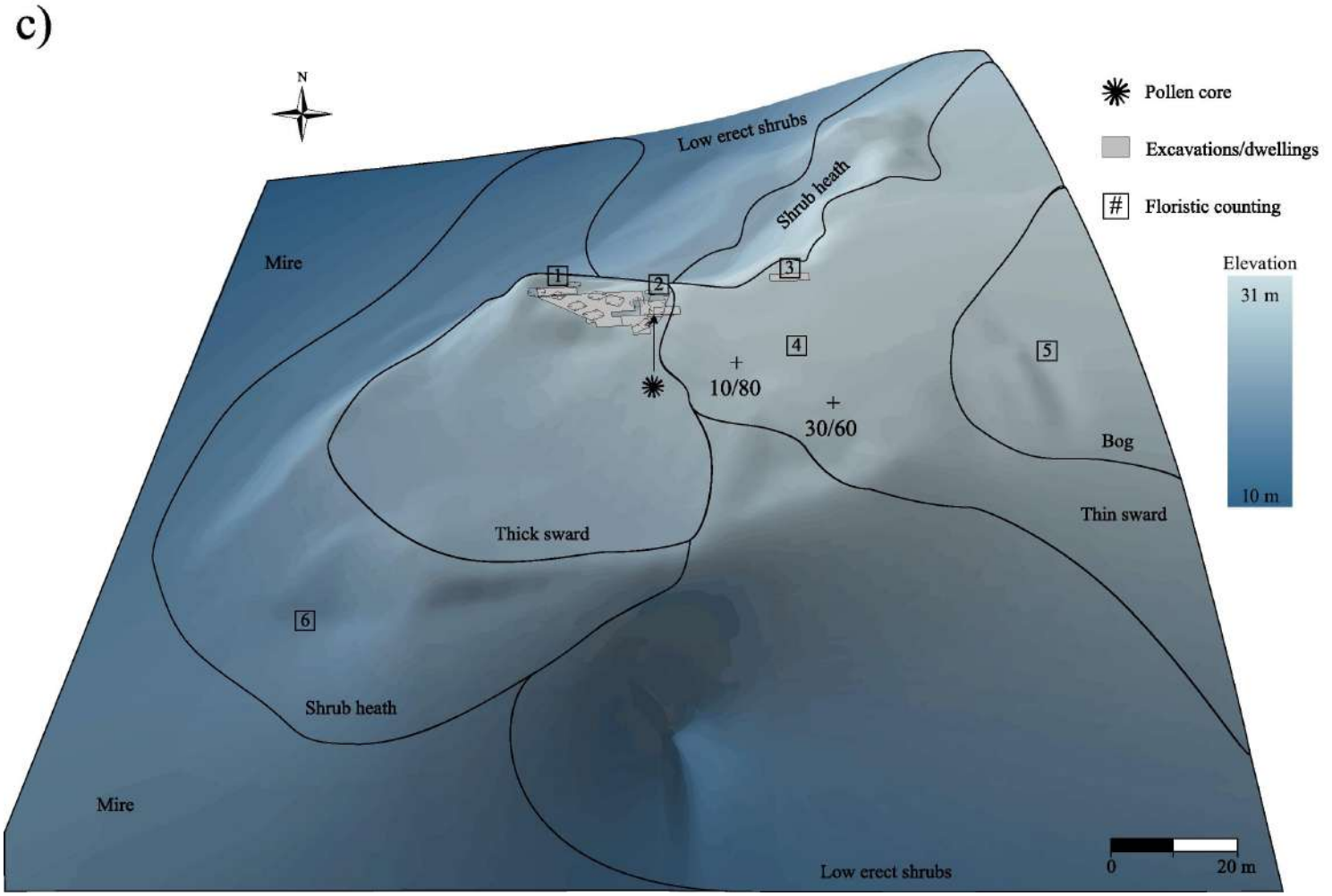
c)
N
Pollen core
Excavations/dwellings
Floristic counting
Elevation
31 m
10 m
Low erect shrubs
Shrub heath
Mire
1
2
3
4
5
6
10/80
30/60
Bog
Thin sward
Thick sward
Shrub heath
Mire
Low erect shrubs
0
20 m

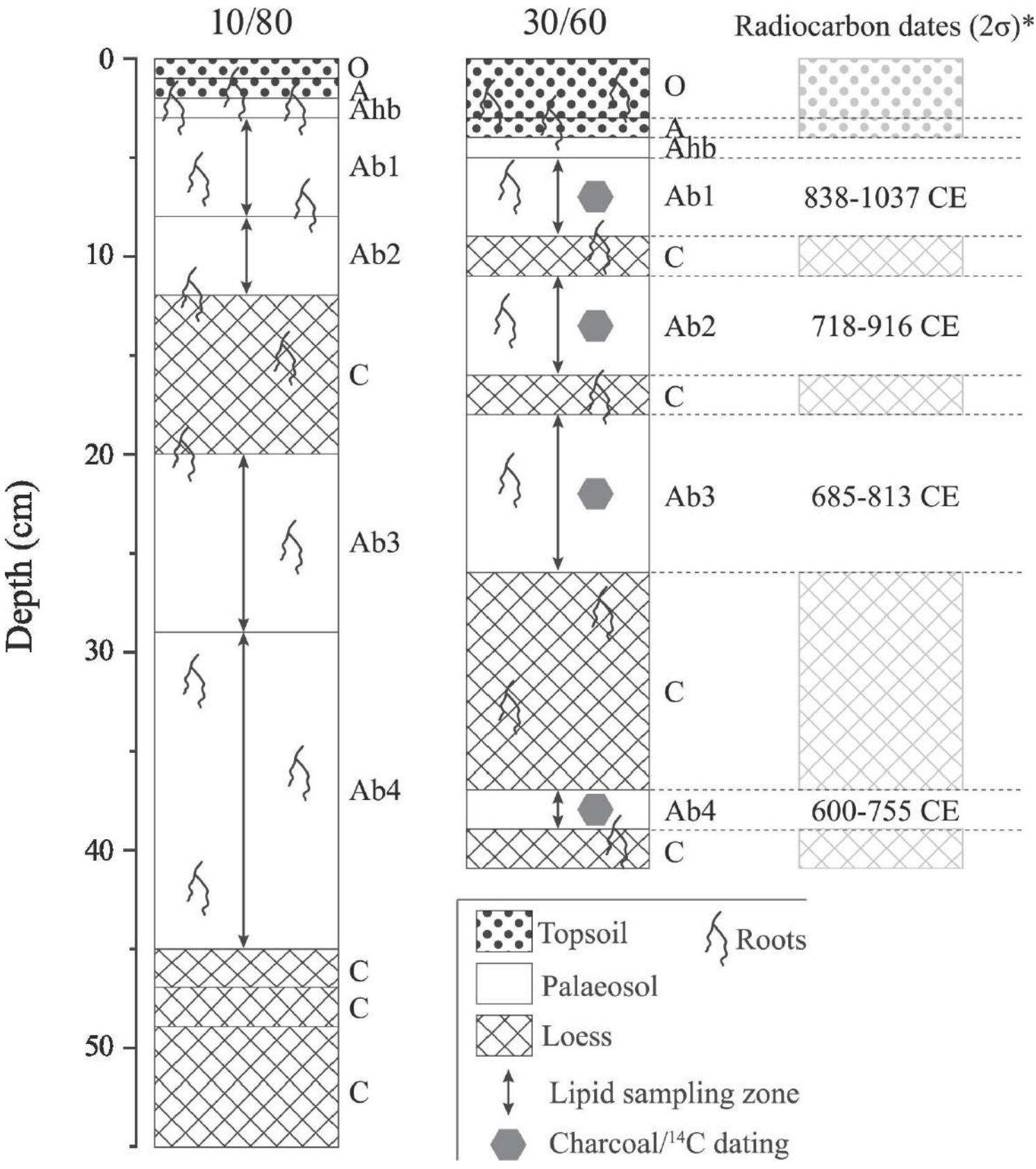
10/80
30/60
Radiocarbon dates (2σ)*
Depth (cm)
0
10
20
30
40
50
O
A
Ahb
Ab1
Ab2
C
Ab3
Ab4
C
C
C
838-1037 CE
718-916 CE
685-813 CE
600-755 CE
Topsoil
Roots
Palaeosol
Loess
Lipid sampling zone
Charcoal/14C dating

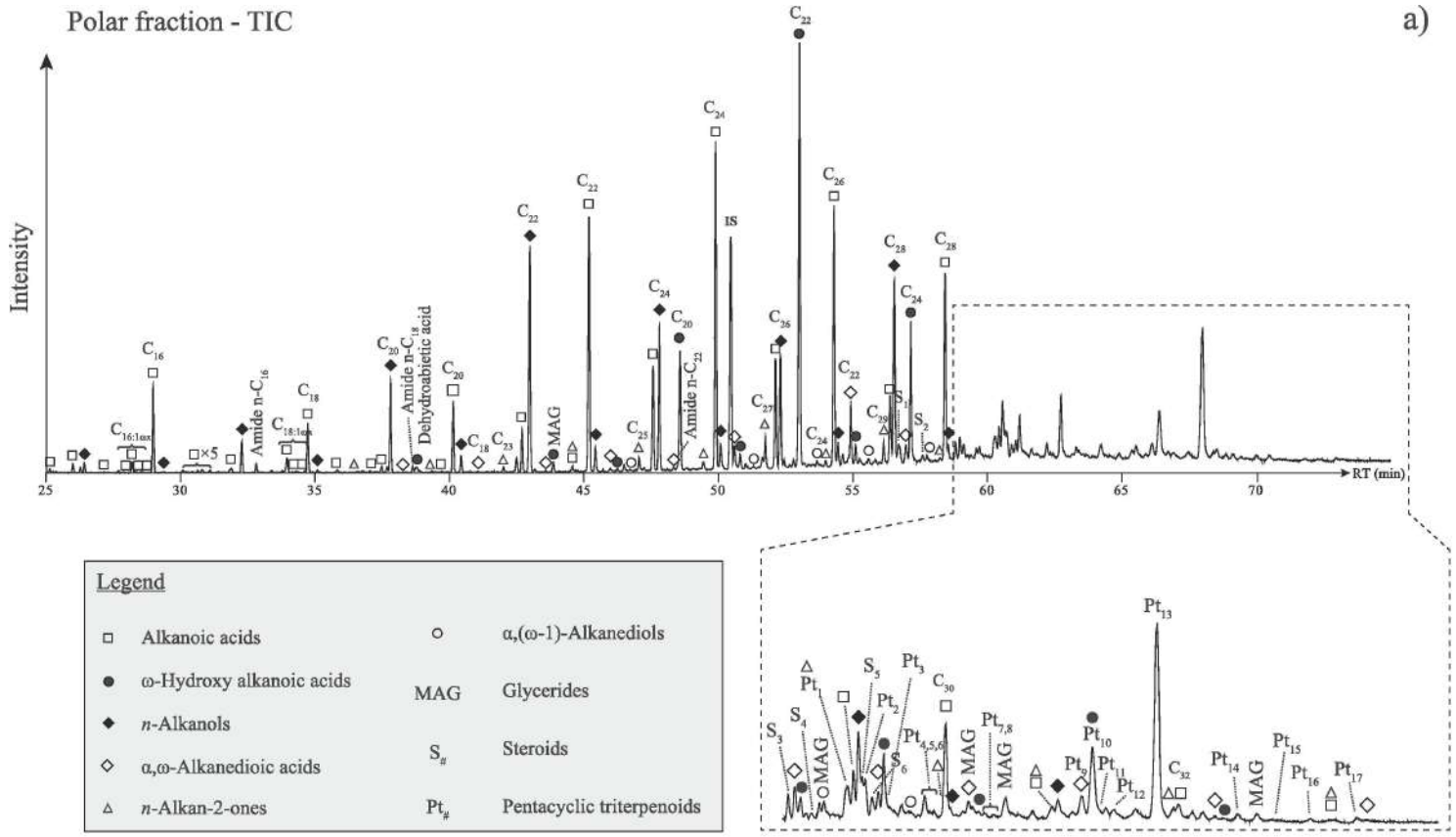
Polar fraction - TIC
a)
Intensity
RT (min)
IS
MAG
Amide n-C16
Amide n-C18
Dehydroabietic acid
Amide n-C22
×5
Legend
Alkanoic acids
ω-Hydroxy alkanoic acids
n-Alkanols
α,ω-Alkanedioic acids
n-Alkan-2-ones
α,(ω-1)-Alkanediols
Glycerides
Steroids
Pentacyclic triterpenoids

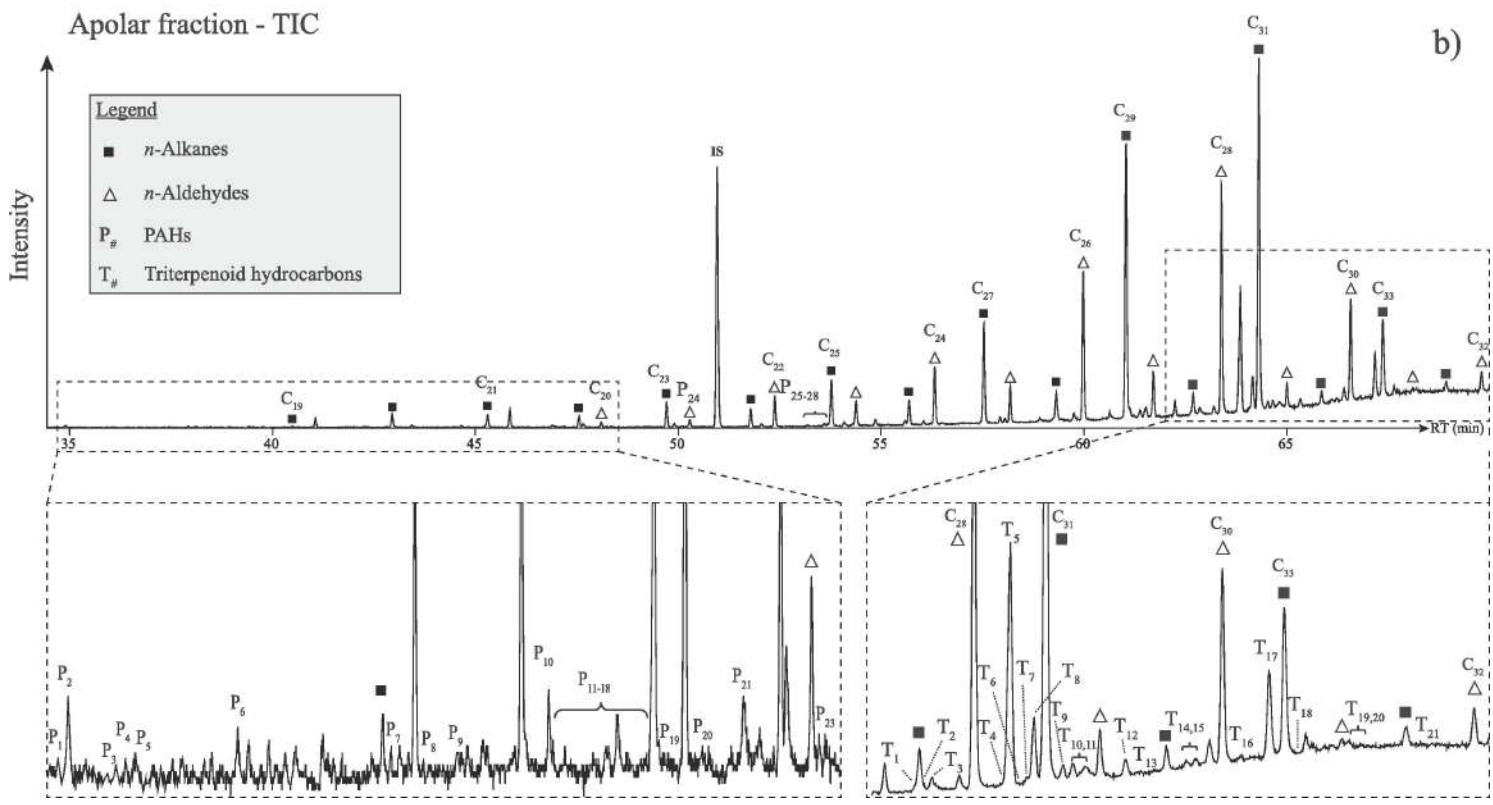
Apolar fraction - TIC
b)
Intensity
RT (min)
IS
Legend
n-Alkanes
n-Aldehydes
PAHs
Triterpenoid hydrocarbons

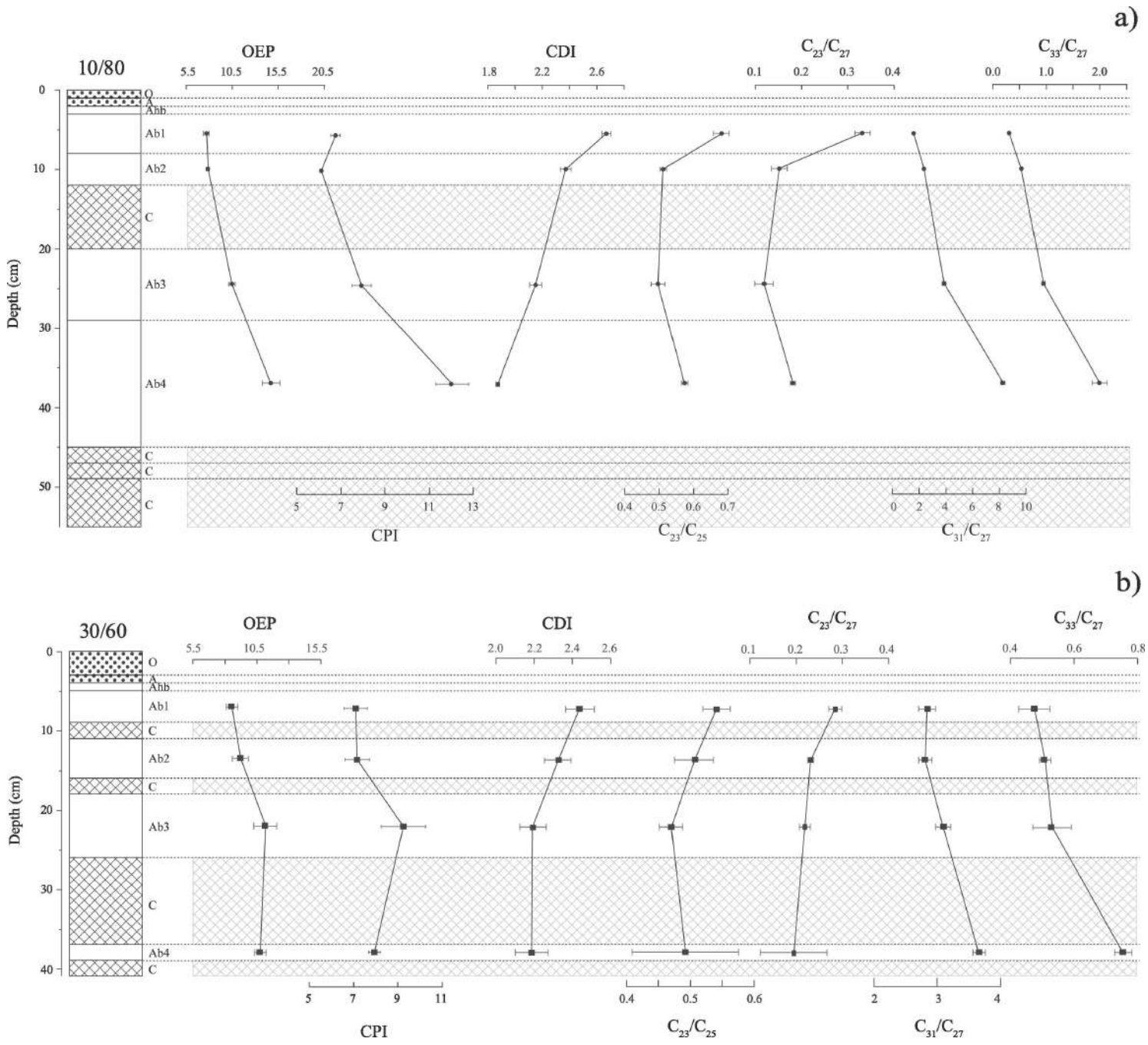
a)
10/80
OEP
CDI
C_{23}/C_{27}
C_{33}/C_{27}
Depth (cm)
O
A
Ahb
Ab1
Ab2
C
Ab3
Ab4
C
C
C
CPI
C_{23}/C_{25}
C_{31}/C_{27}
b)
30/60
OEP
CDI
C_{23}/C_{27}
C_{33}/C_{27}
Depth (cm)
O
A
Ahb
Ab1
C
Ab2
C
Ab3
C
Ab4
C
CPI
C_{23}/C_{25}
C_{31}/C_{27}

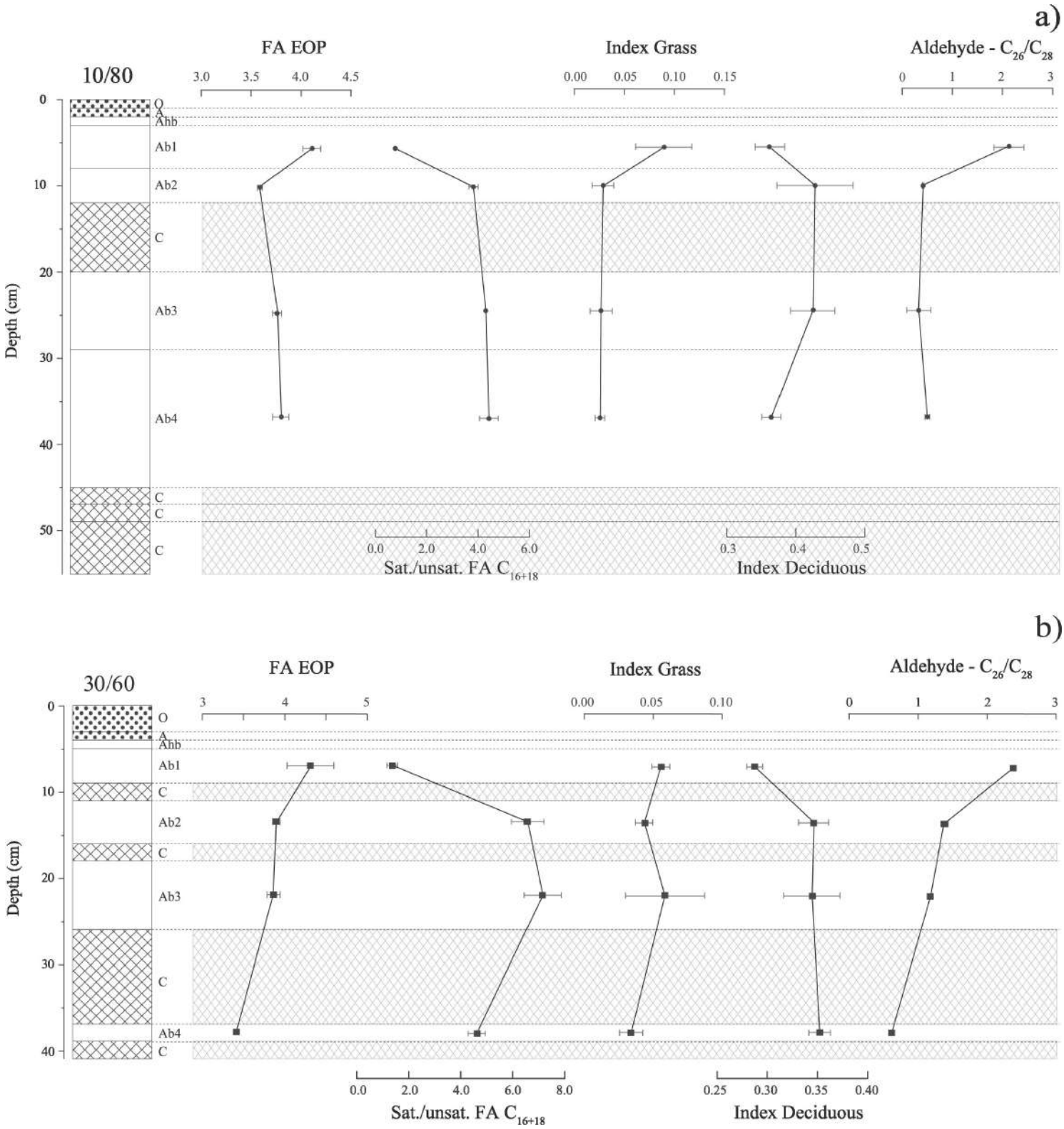
a)
10/80
FA EOP
Index Grass
Aldehyde - C26/C28
Depth (cm)
O
A
Ahb
Ab1
Ab2
C
Ab3
Ab4
C
C
C
Sat./unsat. FA C16+18
Index Deciduous
b)
30/60
FA EOP
Index Grass
Aldehyde - C26/C28
Depth (cm)
O
A
Ahb
Ab1
C
Ab2
C
Ab3
C
Ab4
C
Sat./unsat. FA C16+18
Index Deciduous

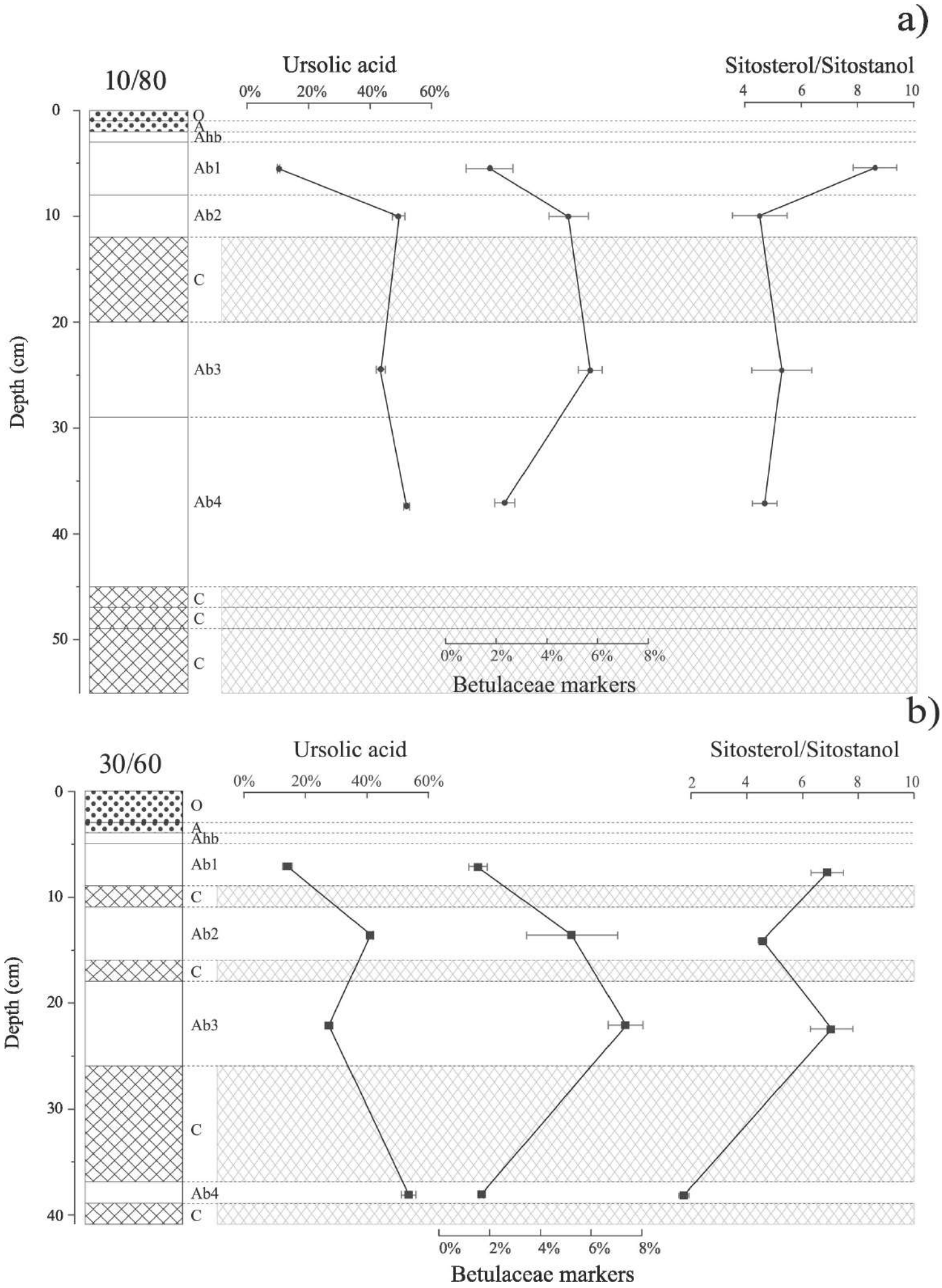
a)
10/80
Ursolic acid
0%
20%
40%
60%
Sitosterol/Sitostanol
4
6
8
10
Depth (cm)
0
10
20
30
40
50
O
A
Ahb
Ab1
Ab2
C
Ab3
Ab4
C
C
C
0%
2%
4%
6%
8%
Betulaceae markers
b)
30/60
Ursolic acid
0%
20%
40%
60%
Sitosterol/Sitostanol
2
4
6
8
10
Depth (cm)
0
10
20
30
40
O
A
Ahb
Ab1
C
Ab2
C
Ab3
C
Ab4
C
0%
2%
4%
6%
8%
Betulaceae markers

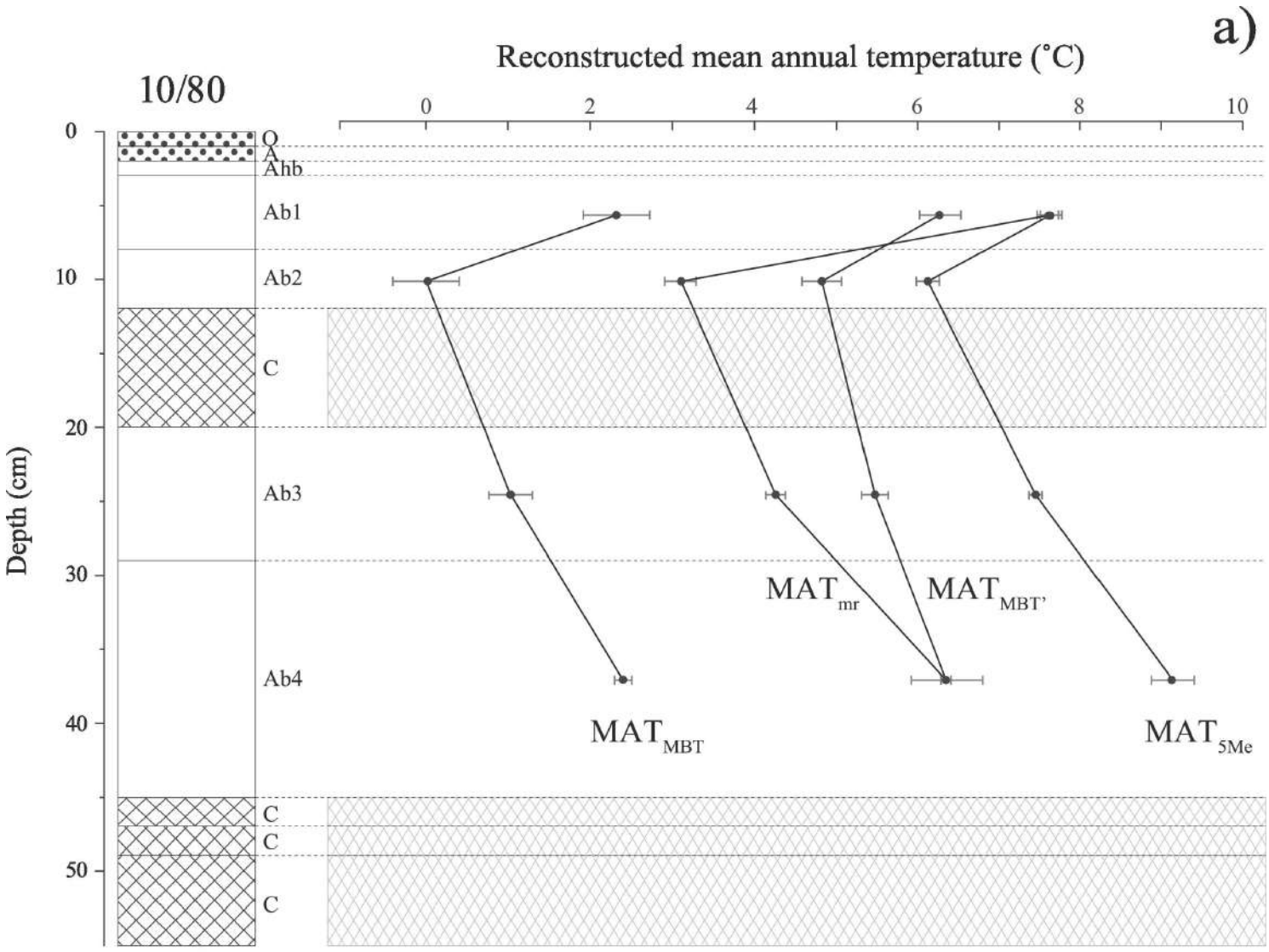
a)
10/80
Reconstructed mean annual temperature (°C)
0
2
4
6
8
10
Depth (cm)
0
10
20
30
40
50
O
A
Ahb
Ab1
Ab2
C
Ab3
Ab4
C
C
C
MAT mr
MAT MBT'
MAT MBT
MAT 5Me

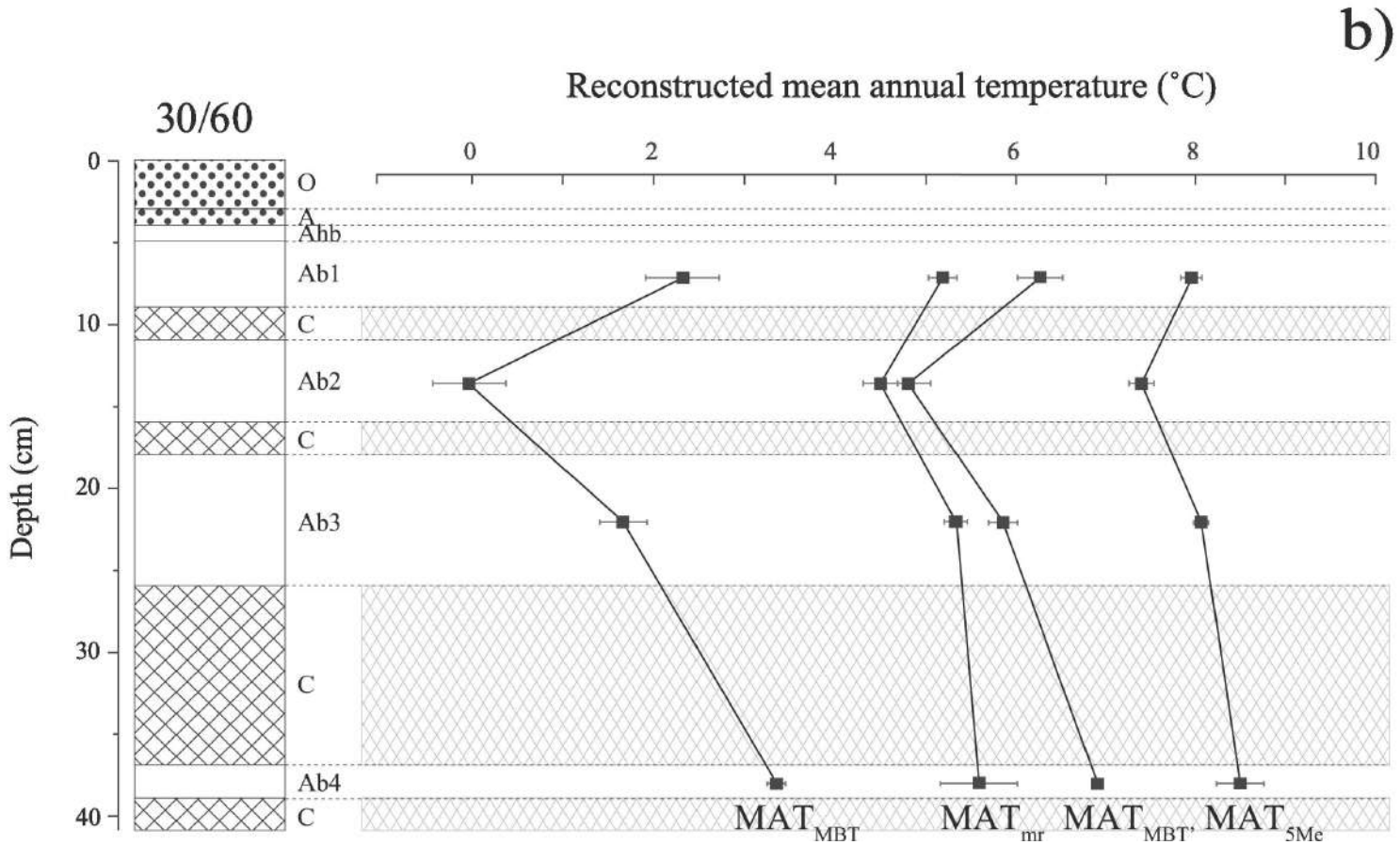
b)
30/60
Reconstructed mean annual temperature (°C)
0
2
4
6
8
10
Depth (cm)
0
10
20
30
40
O
A
Ahb
Ab1
C
Ab2
C
Ab3
C
Ab4
C
MAT MBT
MAT mr
MAT MBT'
MAT 5Me

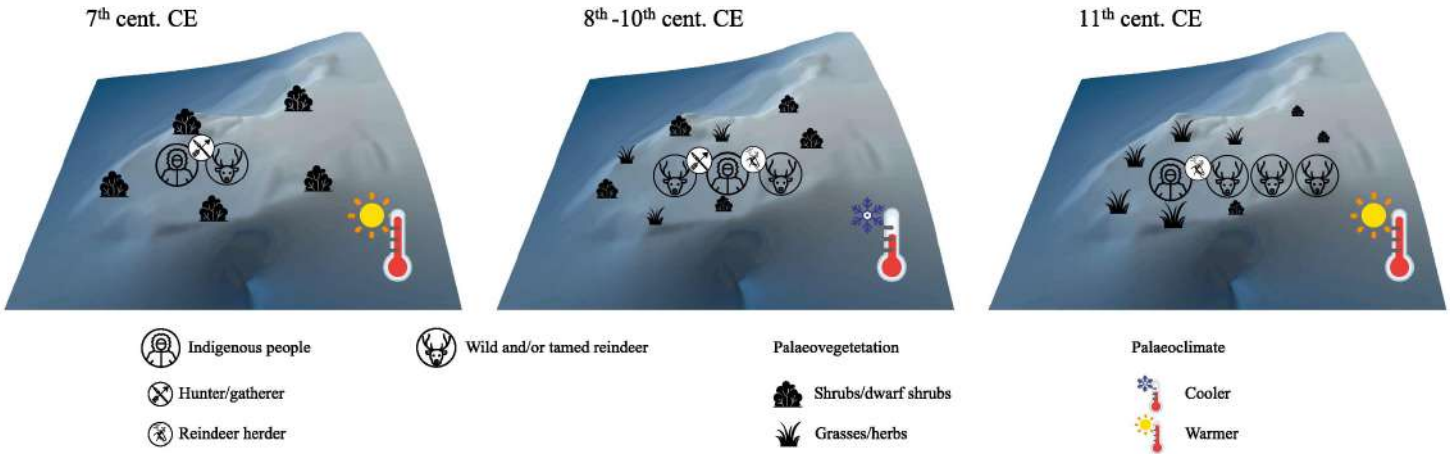
7th cent. CE
8th -10th cent. CE
11th cent. CE
Indigenous people
Hunter/gatherer
Reindeer herder
Wild and/or tamed reindeer
Palaeovegetetation
Shrubs/dwarf shrubs
Grasses/herbs
Palaeoclimate
Cooler
Warmer